

1 **Novel insights into deep groundwater exploration by geophysical estimation of**  
2 **hard rock permeability**

3 **Muhammad Hasan** <sup>1, 2, 3,\*</sup>, **Lijun Su** <sup>1, 2, 3, \*\*</sup>

4 <sup>1</sup> *State Key Laboratory of Mountain Hazards and Engineering Resilience, Institute of Mountain*  
5 *Hazards and Environment, Chinese Academy of Sciences, Chengdu 610299, China*

6 <sup>2</sup> *China-Pakistan Joint Research Center on Earth Sciences, CAS-HEC, Islamabad, Pakistan*

7 <sup>3</sup> *University of Chinese Academy of Sciences, Beijing 100049, China*

8

9 \*Corresponding authors:

10 Muhammad Hasan: Email: [mhasan@imde.ac.cn](mailto:mhasan@imde.ac.cn); ORCID: [https://orcid.org/0000-0001-6804-](https://orcid.org/0000-0001-6804-7962)  
11 [7962](https://orcid.org/0000-0001-6804-7962); Phone Number: +86-13051361710

12 Lijun Su: Email: [sulijun1976@163.com](mailto:sulijun1976@163.com); ORCID: <https://orcid.org/0000-0001-9972-4698>

13 Corresponding authors' postal address: State Key Laboratory of Mountain Hazards and  
14 Engineering Resilience, Institute of Mountain Hazards and Environment, Chinese Academy of  
15 Sciences, Chengdu 610299, China

16

17

18

19

20

21

22

23 **Abstract**

24 Deep groundwater exploration in hard rock terrains is critical in regions where deep aquifers may  
25 offer long-term water security amidst increasing scarcity. However, such exploration is globally  
26 challenged by geological complexity and the limitations of traditional investigative techniques.  
27 Accurate estimation of hydraulic parameters, particularly permeability ( $k$ ), is essential for  
28 effective groundwater management and future resource planning. Conventional borehole-based  
29 methods for measuring  $k$  are invasive, costly, time-consuming, and limited to sparse, point-scale  
30 observations, making them inadequate for characterizing deep and heterogeneous aquifer  
31 systems. ~~In contrast, geophysical methods offer a non-invasive, cost-effective, and efficient  
32 alternative, enabling large-scale assessment of subsurface hydrogeological conditions with  
33 minimal surface disruption. Previous geophysical studies have employed empirical approaches,  
34 particularly vertical electrical sounding (VES), to estimate permeability. However, these  
35 methods are confined to shallow depths, homogeneous settings, and one-dimensional  
36 interpretation, making them insufficient for application in highly heterogeneous hard-rock  
37 environments. This study introduces, for the first time, the use of controlled-source audio-  
38 frequency magnetotellurics (CSAMT) to estimate two and three-dimensional permeability  
39 distributions at depths exceeding 1 km in complex geological settings, including sedimentary,  
40 igneous, and metamorphic rocks. The results demonstrate that CSAMT can effectively  
41 characterize deep subsurface variability and generate accurate, spatially continuous  
42 hydrogeological models in hard-rock terrains, particularly where drilling data are limited or  
43 unavailable. Our approach cuts down on the need for costly borehole tests and allows for a more  
44 thorough assessment of aquifer potential. This research provides a major breakthrough in deep  
45 groundwater investigation and helps with better scientific planning and long-term groundwater~~

**Formatted:** Space After: 10 pt, Tab stops:  
Not at 0.64" + 1.27" + 1.91" + 2.54" +  
3.18" + 3.82" + 4.45" + 5.09" + 5.73" +  
6.36" + 7" + 7.63" + 8.27" + 8.91" + 9.54"  
+ 10.18"

46 ~~resource management in challenging hard rock areas~~ Geophysical methods offer a promising  
47 non-invasive alternative, enabling broader spatial coverage with reduced surface disturbance.  
48 While previous studies have used empirical approaches, such as vertical electrical sounding  
49 (VES), to estimate  $k$ , these techniques are typically constrained to shallow depths (typically <200  
50 m), homogeneous conditions, and one-dimensional interpretations. This study advances the  
51 application of resistivity-based geophysical methods by demonstrating, for the first time, the use  
52 of controlled-source audio-frequency magnetotellurics (CSAMT) to estimate two- and three-  
53 dimensional  $k$  distributions to depths exceeding 1 km across complex geological settings,  
54 including sedimentary, igneous, and metamorphic formations. In doing so, it extends the scope  
55 of earlier hydrogeophysical research, which has largely focused on shallower or more uniform  
56 subsurface environments. The results show that, when calibrated with borehole data, CSAMT  
57 can reliably capture deep subsurface variability and produce spatially continuous  
58 hydrogeological models in hard rock terrains, particularly in areas with limited borehole  
59 coverage. While CSAMT inversion is inherently ill-posed, the incorporation of ground-truth data  
60 significantly enhances model robustness and interpretability. This integrated approach reduces  
61 dependence on extensive borehole drilling and enables broader and more economical evaluation  
62 of aquifer potential. The methodology represents a significant advancement in deep groundwater  
63 exploration and offers valuable insights for sustainable groundwater resource management and  
64 long-term water security in geologically complex hard rock regions.

Formatted: Font: (Default) Times New Roman, 12 pt

Formatted: Font: Italic

Formatted: Font: (Default) Times New Roman, 12 pt

Formatted: Font: (Default) Times New Roman, 12 pt

Formatted: Font: Italic

Formatted: Font: (Default) Times New Roman, 12 pt

Formatted: Font: (Default) Times New Roman, 12 pt

Formatted: Font: (Asian) +Body Asian, Not Bold, Font color: Auto

65 **Keywords:** Permeability; Geophysical methods; Hydraulic parameters; Groundwater; Hard rock;  
66 Hydrogeological models

## 67 **1 Introduction**

68 Metamorphic and igneous rocks dominate Earth's crust and cover about one-third of its surface  
69 ([Amiotte Suchet et al., 2003](#)). In hard rock terrains, groundwater research focuses on delineating  
70 subsurface structures, such as faults and fractures that control water storage and flow ([Fernando  
71 and Pacheco, 2015](#); [Hasan et al., 2021](#)). A key parameter in this context is aquifer potential,  
72 which reflects the capacity of rock formations to store and transmit groundwater and is  
73 influenced by lithology, structural complexity, mineral composition, weathering, and infiltration  
74 depth ([Majumdar and Das, 2011](#); [Zhu et al., 2017](#)). However, accurately characterizing the  
75 lateral and vertical heterogeneity of these properties remains challenging due to limited data and  
76 the complexity of massive rock units ([Dewandel et al., 2006](#)). In such settings, conventional  
77 methods often fall short, leading to inefficient or unsustainable groundwater development  
78 ([Nwosu et al., 2013](#); [Worthington et al., 2016](#)). Developing cost-effective and reliable  
79 approaches for subsurface assessment is therefore essential for managing groundwater in hard  
80 rock environments.

81 Groundwater at depths beyond 500 m is typically isolated from surface hydrological  
82 influences and often exhibits brackish or saline characteristics ([Ferguson et al., 2023](#)). Its  
83 strategic importance is increasingly recognized, particularly in geologically and environmentally  
84 constrained settings ([Gleeson et al., 2014](#)). In the Jinji region, several factors necessitate focused  
85 investigation of deep aquifers. Surface water is scarce and unreliable, while the shallow  
86 subsurface is dominated by fresh granite, which has inherently low porosity and permeability,  
87 limiting groundwater availability. By contrast, deeper fractured zones in granite, sandstone, and  
88 hornstone present more favorable hydrogeological conditions. Recent national water initiatives  
89 in China have emphasized deep subsurface exploration in structurally complex terrains to  
90 identify underutilized aquifers for enhancing long-term water security. Comprehensive

91 assessment of these deep reserves is essential to evaluate their recharge potential and integrate  
92 them into sustainable resource management strategies (Condon et al., 2020; Hasan and Shang,  
93 2022). As pressure on surface and shallow groundwater intensifies, deep aquifers may serve as a  
94 vital buffer against increasing environmental and socio-economic stress.

95 Multiple studies have documented the rapid depletion of global groundwater reserves,  
96 raising serious concerns about long-term water sustainability (Wada et al., 2010; Laghari et al.,  
97 2012; Jasechko et al., 2024). Addressing this challenge requires accurate and detailed  
98 assessments of groundwater resources, which depend critically on a clear understanding of  
99 subsurface hydraulic properties. ~~Permeability is a crucial parameter for characterizing the ability  
100 of geological formations to store and transmit water~~ Permeability ( $k$ ) is a key parameter that  
101 describes the ease with which fluids can move through a porous medium, while the capacity to  
102 store water is more directly characterized by porosity. This parameter is crucial for aquifer  
103 analysis in various hydrogeological settings (Allègre et al., 2016; Esmailpour et al., 2023;  
104 Carbillet et al., 2024). Borehole testing remains the standard method for estimating  $k$  and related  
105 aquifer parameters (De Lima and Niwas, 2000; Hasan et al., 2021). However, borehole  
106 investigations are often limited by high costs, logistical challenges, and poor spatial coverage,  
107 particularly in rugged terrains, while offering only localized information with limited ability to  
108 image lateral and deep structures (Singh, 2005; Fiandaca et al., 2018). These limitations  
109 contribute to uncertainties in groundwater assessments, especially in data-scarce regions (Hasan  
110 and Shang, 2022). ~~Alternatively, it is essential to develop methods that minimize the reliance on  
111 costly drilling while still enabling accurate evaluation of groundwater storage capacity within  
112 prospective rock formations~~ Alternatively, it is essential to develop methods that minimize

Formatted: Font: Italic

113 reliance on costly drilling while still enabling reliable estimation of permeability within  
114 prospective rock formations.

115 Geophysical methods are widely and effectively employed to enhance subsurface  
116 characterization in groundwater studies (Daily et al., 1992; Jardani et al., 2007; Hinnell et al.,  
117 2010; Fu et al., 2013; Jiang et al., 2014; Kouadio et al., 2023). Compared to conventional  
118 drilling, these techniques offer significant advantages in cost, deployment speed, environmental  
119 impact, and spatial extent (Hu et al., 2013; Fusheng et al., 2022). Their ability to image both  
120 vertical and lateral subsurface variations makes them particularly effective in heterogeneous  
121 terrains (Hasan et al., 2025). Among them, resistivity-based methods are widely used due to their  
122 sensitivity to lithology, porosity, fractures, and fluid content (Hasan et al., 2021; Asfahani,  
123 2023). Common techniques include electrical resistivity tomography (ERT), vertical electrical  
124 sounding (VES), and electromagnetic methods such as magnetotellurics (MT), time-domain  
125 electromagnetics (TDEM), and controlled-source audio-frequency magnetotellurics (CSAMT)  
126 (Soupios et al., 2007; Bauer-Gottwein et al., 2010; Pollock and Cirpka, 2012; Jiang et al., 2014;  
127 Di et al., 2020). VES offers a budget-friendly solution for shallow 1D (one-dimensional)  
128 profiling (typically <200 m) but lacks lateral resolution in complex settings (Niwas and De Lima,  
129 2003; Majumdar and Das, 2011). ERT offers improved 2D (two-dimensional) and 3D (three-  
130 dimensional) imaging up to ~300 m depth, making it suitable for fractured and karst systems;  
131 though it requires more field effort and is less effective in extreme resistivity conditions (Abbas  
132 et al., 2022; Hasan and Shang, 2022). For deeper targets, electromagnetic methods such as  
133 TDEM, MT, and CSAMT are often employed (Bauer-Gottwein et al., 2010; Di et al., 2020;  
134 Gonzalez-Duque et al., 2024). MT provides excellent depth penetration (up to tens of kilometers)  
135 and is widely used in regional-scale studies and geothermal exploration, though it requires long

136 [acquisition times and is sensitive to cultural noise \(Simpson and Bahr, 2005\). TDEM offers a](#)  
137 [compromise between resolution and depth, reaching several hundred meters with rapid](#)  
138 [deployment, but can be constrained by near-surface conductivity and limited sensitivity at](#)  
139 [greater depths \(Bauer-Gottwein et al., 2010\). CSAMT, by contrast, bridges the gap between](#)  
140 [these methods. With controlled-source signals and frequency tuning, CSAMT enables high-](#)  
141 [resolution 2D and 3D imaging of conductive structures over 1,000 m depth, even in culturally](#)  
142 [noisy and geologically complex settings \(Smith and Booker, 1991; Zhang et al., 2021\).](#) Although  
143 its spatial resolution is generally lower than ERT, CSAMT offers superior performance for deep  
144 hydrogeological investigations, especially when integrated with borehole data and empirical  
145 modeling (Zonge and Hughes, 1991; Wang et al., 2015). The choice between resistivity and  
146 electromagnetic techniques is contingent upon parameters like investigation depth, resolution  
147 requirements, geological complexity, and logistical constraints (Majumdar and Das, 2011; Hasan  
148 et al., 2025). Given the objectives of this study, to delineate deep aquifer structures in a hard rock  
149 setting, CSAMT was selected as the most suitable method, offering a practical balance of depth  
150 penetration, imaging capability, and field adaptability.

151 In fractured rocks like granite, metamorphic, and sandstone formations, fluid flow is  
152 largely controlled by fracture networks rather than matrix porosity. Accurate hydraulic  
153 assessment in such settings benefits from integrated geophysical and hydrogeological approaches  
154 to better capture spatial variability and improve flow modeling (Hasan et al., 2021; Abbas et al.,  
155 2022). Resistivity-based techniques are particularly valuable for delineating subsurface structures  
156 and identifying water-bearing zones. Because electrical resistivity is sensitive to porosity,  
157 saturation, fracture density, and fluid salinity, it is increasingly used to infer  $k$  in heterogeneous  
158 geological settings (Mudunuru et al., 2022; Yan et al., 2024). Numerous parameters significantly

159 ~~affect hydraulic properties, highlighting the utility of resistivity measurements as indicators for~~  
160 ~~evaluating groundwater flow potential~~ Permeability is influenced by numerous parameters,  
161 ~~including porosity, fracture density and orientation, grain size distribution, degree of weathering,~~  
162 ~~pore connectivity, and saturation level, highlighting the utility of resistivity measurements as~~  
163 ~~indicators for evaluating groundwater flow potential~~ (Gerke et al., 2011; Worthington et al.,  
164 ~~2016; Pellet et al., 2024).~~

165 Empirical and semi-empirical models have been developed to estimate hydraulic  
166 ~~properties from geophysical measurements, particularly in data-sparse regions~~ (Niwas and De  
167 ~~Lima, 2003; Singh, 2005; Soupios et al., 2007; Hasan et al., 2021; Asfahani, 2023). In parallel,~~  
168 ~~resistivity-based methods and hydrogeophysical inversion techniques have been developed to~~  
169 ~~more rigorously estimate hydraulic parameters by integrating petrophysical relationships within~~  
170 ~~geophysical modeling frameworks~~ (Daily et al., 1992; Ferré et al., 2009; Binley et al., 2010;  
171 ~~Hinnell et al., 2010; Herckenrath et al., 2012; Pollock and Cirpka, 2012; Herckenrath et al.,~~  
172 ~~2013; Binley et al., 2015). These approaches have improved resolution in parameter estimation,~~  
173 ~~particularly in shallow, unconsolidated, or relatively homogeneous settings. However,~~  
174 ~~applications to deep, fractured, and lithologically complex environments remain limited,~~  
175 ~~especially in terms of producing volumetric  $k$  models at kilometer-scale depths. Despite these~~  
176 ~~advances, generation of detailed 2D and 3D  $k$  maps from resistivity data in deep, hard-rock~~  
177 ~~terrains is constrained by limited borehole control, significant geological heterogeneity, and the~~  
178 ~~ill-posed nature of geophysical inversion. In such contexts, integrating resistivity data with~~  
179 ~~borehole measurements presents a practical, cost-effective solution for characterizing aquifer~~  
180 ~~properties over large areas and depth ranges. This study builds on prior hydrogeophysical~~  
181 ~~research and introduces a novel application of the CSAMT method for volumetric  $k$  modeling in~~

Formatted: Font: Italic

Formatted: Font: Italic

Formatted: Font: Italic

182 a complex, fractured hard-rock setting. While previous studies have applied resistivity-based  
183 techniques to estimate hydraulic properties, this is the first to utilize CSAMT for constructing the  
184 detailed 2D and 3D  $k$  modeling beyond 1000 m depth in geologically heterogeneous terrains  
185 comprising hornstone, granite, and sandstone. Few available drilling tests were used to calibrate  
186 CSAMT-derived resistivity with laboratory-measured  $k$ , allowing the resulting empirical  
187 relationship to be applied across the broader survey domain. Several CSAMT profiles were  
188 conducted along and beyond the borehole locations, and the calibrated resistivity–permeability  
189 correlation was used to generate spatially continuous subsurface models in regions lacking direct  
190 borehole data. This integration resulted in a robust, data-constrained workflow capable of  
191 revealing  $k$  variations across diverse rock units and lithological boundaries. The method offers a  
192 practical and scalable alternative to extensive drilling campaigns, enabling a more detailed and  
193 cost-efficient evaluation of deep groundwater potential in structurally complex terrains.

Formatted: Font: Italic

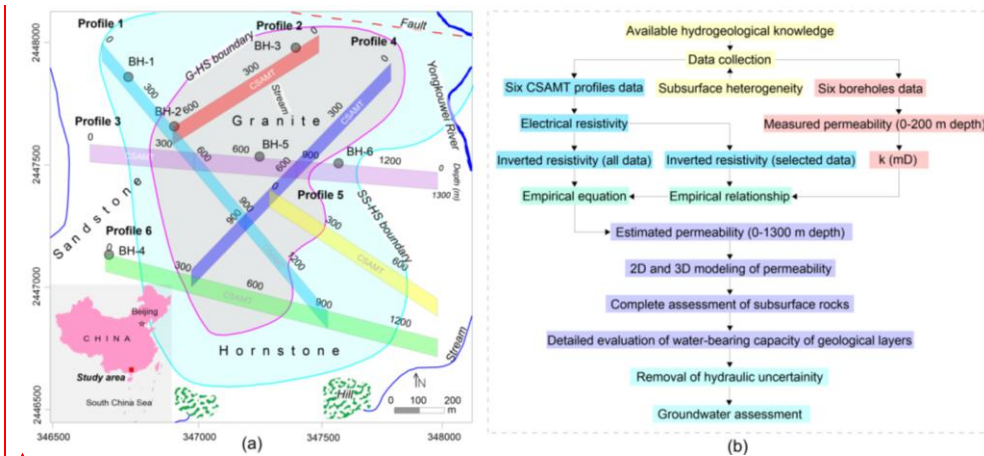
Formatted: Font: Italic

Formatted: Font: Italic

194 Ultimately, this work extends the scope of hydrogeophysical methods by demonstrating  
195 the feasibility of applying CSAMT for deep hydraulic parameter estimation in hard rock. It  
196 bridges a critical methodological gap in hard-rock hydrogeology and sets the foundation for  
197 future CSAMT-based volumetric modeling in similarly challenging environments. This study  
198 aims to develop and apply a geophysical-based approach for mapping the spatial distribution of  $k$   
199 in deep, hard-rock settings. By integrating CSAMT data with targeted borehole measurements,  
200 this research enhances 2D and 3D hydrogeological assessments across heterogeneous lithologies  
201 in structurally complex terrains. It also minimizes reliance on extensive drilling, demonstrating  
202 the value of non-invasive geophysical techniques as a cost-effective alternative for deep  
203 groundwater exploration.

## 204 **2 Methods**

205 This research integrates inadequate drilling information with the geophysical data to estimate  $k$   
 206 for both 2D and 3D evaluations of groundwater resources over the entire investigated site (Fig.  
 207 1a). The main stages of the methodology are summarized in the flowchart shown in Fig. 1b.



208 **Fig. 1.** (a) The site map displaying six boreholes (BH-1 to BH-6) and six CSAMT survey profiles (1–6).  
 209 The map also illustrates the simplified geological and hydrogeological setting, including the dominant  
 210 rock types (granite, hornstone, and sandstone), the granite–hornstone (G–HS) and sandstone–hornstone  
 211 (SS–HS) boundaries, major fault lines, streams, rivers, and surrounding mountainous terrain; (b)  
 212 Flowchart illustrating the methodology for generating 2D and 3D  $k$  models to enable comprehensive  
 213 assessments of groundwater resources across extensive areas

215 **2.1 Study area and hydrogeological settings**

216 This study is part of a national initiative in South Guangdong, China, focused on deep  
 217 subsurface exploration, including groundwater resource assessment and infrastructure  
 218 development such as the Jiangmen Underground Neutrino Observatory (JUNO) (Hasan et al.,  
 219 2025). These actions contribute to China's national agenda toward sustainable deep-earth

Formatted: Font: (Default) Times New Roman, 12 pt, Bold

Formatted: Font: 11 pt

Formatted: Font: 11 pt

220 resource utilization. This research was conducted in the Jinji region, a geologically complex area  
221 prioritized for deep groundwater exploration (Fig. 1a). The region lies within a subtropical  
222 monsoonal climate zone, receiving ~1981 mm of annual rainfall. Topography ranges from low  
223 hills to mountainous terrain (39–539.9 m elevation), with dense vegetation and varied slopes.  
224 The northern part is relatively flat, while the south includes prominent features such as the  
225 Dashishan and Qilongding Mountains. Surface drainage is primarily controlled by the  
226 Yongkouwei River in the northeast.

227 Geologically, the Jinji area has evolved through successive tectono-magmatic processes  
228 linked to the Yanshanian, Indosinian, and Caledonian mountain-building phases, resulting in a  
229 lithologically diverse landscape of granite, sandstone, and hornstone (Qin, 2017). Granite  
230 intrusions reflect deep crustal magmatism, while hornstone indicates contact metamorphism.  
231 Overlying Paleogene sediments record later basin development. Tectonic structuring in the area  
232 is largely influenced by the Kaiping fault-fold complex, which includes reverse, thrust, and  
233 strike-slip faults formed under prolonged crustal compression and later modified by strike-slip  
234 tectonics. These northeast-trending structures govern subsurface architecture and groundwater  
235 flow pathways (Yang et al., 2021). Fractures and joints are widespread in granite, sandstone, and  
236 hornstone, varying by lithology and tectonic history. These brittle features act as primary  
237 conduits for groundwater, with their alignment along major faults highlighting the tight coupling  
238 between structural geology and hydrogeology.

239 This study focuses on the vertical stratification of aquifer-bearing formations. Productive  
240 groundwater is mainly stored in deep, fractured sandstone units, overlain by low-permeability  
241 granite that limits vertical recharge. An intermediate hornstone layer separates the two, with  
242 moderate hydraulic properties and limited connectivity. This configuration isolates the deep

243 aquifer from surface influences, rendering shallow investigations ineffective. Deep-targeted  
244 exploration is thus essential for identifying and managing these concealed high-potential  
245 groundwater resources in a structurally complex hard rock setting.

## 246 **2.2 CSAMT survey**

### 247 **2.2.1 Theoretical background**

248 CSAMT is extensively employed for hard rock evaluations due to its ability to resolve deep  
249 subsurface features (Fu et al., 2013; Wang et al., 2015; Di et al., 2020; Kouadio et al., 2023).  
250 This method employs a distant, regulated electric source that transmits signals into the ground,  
251 while electric and magnetic field components are recorded at receiving stations (Zonge and  
252 Hughes, 1991). CSAMT uses frequency-dependent EM wave penetration; lower frequencies  
253 reach greater depths, depending on rock conductivity (Cagniard, 1953; Borah and Patro, 2019).  
254 Signal frequencies are extracted using Fourier transforms from time-series field measurements  
255 (Simpson and Bahr, 2005). A typical CSAMT setup uses electric dipole sources arranged  
256 between 1 and 2 km intervals, with 5–10 km offsets based on the required penetration depth and  
257 lithological conditions.

258 Resistivity is calculated by analyzing orthogonal electric and magnetic field magnitudes.  
259 Vertical resolution typically ranges from 5%–20% of the depth of investigation (DOI), which  
260 spans ~20–1000 m. Shallow depths (20–100 m) offer finer resolution, while deeper imaging is  
261 coarser due to signal attenuation. DOI increases with lower frequencies and higher subsurface  
262 resistivity (Borah and Patro, 2019). Lateral resolution depends on station spacing (10–200 m);  
263 wider spacing enhances signal strength and coherence (Simpson and Bahr, 2005). Field setups  
264 include portable receivers with electrodes and magnetic sensors to record signals, which are

265 filtered and amplified in real time. Effective survey planning is essential to mitigate interference  
266 from fences, power lines, and radio transmitters. Final resistivity models are presented in plan,  
267 fence, cross-sectional, or 3D formats.

### 268 2.2.2 Survey design and procedures

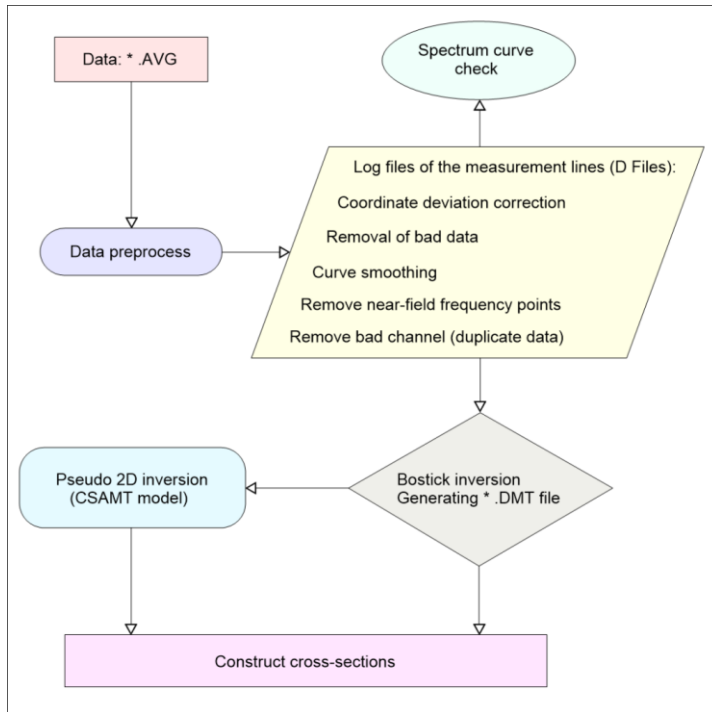
269 Data acquisition was performed along six CSAMT lines (1–6) using a 50 m interval between  
270 stations, selected based on geological targets, terrain accessibility, structural orientation,  
271 integration with borehole data, and expected resistivity contrasts. These optimized profiles  
272 improved subsurface resolution and minimized interpretational ambiguity. The DOI reached  
273 approximately 1300 m. Measurements were conducted in scalar Transverse Magnetic (TM)  
274 mode, recording E- and H-field vectors in both longitudinal and transverse directions along the  
275 survey profiles. EMAP stations were spaced ~50 m from electrodes. A 50 Hz linear filter was  
276 implemented under Gain Mode X1 settings. Transmission current spanned 2.6–18 A across the  
277 7680 Hz to 1 Hz range.

278 Data acquisition utilized a Phoenix Geophysics V8 multifunction receiver and TXU-30  
279 transmitter, capable of 30 kW output, transmitting up to 1000 V and 40 A. The system operated  
280 across 34 frequencies (1–7680 Hz), with transmitter–receiver distances of 9.3–12.5 km. Non-  
281 polarized electrodes captured electric fields, while magnetic fields were recorded using AMTC-  
282 30 sensors (0.1–10,000 Hz). Each site recorded two orthogonal electric and three orthogonal  
283 magnetic components, enabling full impedance tensor calculation. Survey positions were  
284 determined using Hi-Target V30 RTK and Trimble XH GPS, ensuring sub-meter accuracy.  
285 Coordinates were computed and transmitted to the navigation system for real-time positioning.  
286 Survey point spacing remained consistent, with system quality metrics indicating 3–5%  
287 variability. Design tolerances were met: RMS error < ±5%, inter-point error < 10%, horizontal

288 and vertical tolerances of 2.33 mm and 1.67 mm, respectively. Minimal anthropogenic and  
289 electrical interference at the site resulted in high-quality data. Final site interpretation was based  
290 on rigorous CSAMT data processing, including skew filtering and curve analysis ([Hasan et al.,](#)  
291 [2025](#)).

### 292 **2.2.3 Processing workflow**

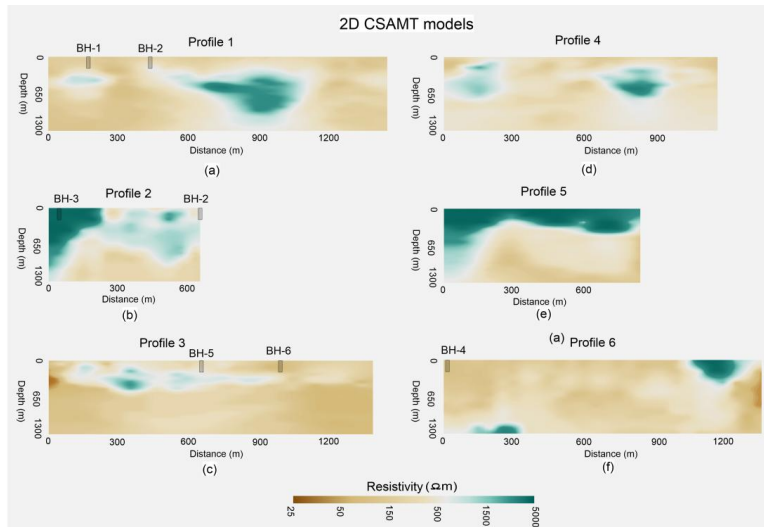
293 Spatial filters (Hanning window) and static corrections were applied to refine resistivity data and  
294 enhance the model accuracy. The static corrections addressed near-surface resistivity  
295 inhomogeneities that cause vertical shifts in apparent resistivity curves. By calibrating electric  
296 field measurements to a stable reference, shallow-layer effects were minimized, isolating deeper  
297 signals. Spatial filtering using a Hanning window reduced high-frequency noise while preserving  
298 coherent spatial patterns. This approach significantly improved inversion model stability by  
299 suppressing spectral leakage and smoothing fluctuations. Data processing was carried out using  
300 the CMTPro version software produced by Phoenix Geophysics ([Phoenix Geophysics CMTPro,](#)  
301 [2020](#)), which integrates V8 and tracking data, corrects coordinates, smoothes curves, and exports  
302 files for inversion. Based on CSAMT-SW technique, the processing workflow shown in [Fig. 2](#)  
303 ([Phoenix Geophysics CSAMT-SW, 2020](#)) was conducted to obtain 2D inversion ([Rodi and](#)  
304 [Mackie, 2001](#); [Wang et al., 2015](#)).



305

306 **Fig. 2.** Schematic of the 2D CSAMT data inversion workflow using Bostick methodology

307 The main components of the CSAMT-SW framework are: 1. Transformation from AVG  
 308 to D format; 2. Editing CHK data and converting to D format; 3. Manual data checks: gap filling,  
 309 near-field removal; 4. Smoothing based on D-format data; 5. Estimation of correction factors (D,  
 310 H, K, Z); 6. The Bostick inversions; 7. The Quasi-2D inversions using the global field model  
 311 (ID), integrating near and transition fields. Post-Bostick inversion results were stored as  
 312 \*\_BOS.DAT and \*\_BSS.DAT, with final inversion-ready data in \*\_M.DMT. The 2D inversion  
 313 proceeded until either the RMS error threshold or a five-iteration limit was reached. Final  
 314 resistivity models (Fig. 3) were cross-validated with local geology and clearly delineated  
 315 subsurface features, offering a robust interpretation framework.



316  
 317 **Fig. 3.** Construction of 2D CSAMT models along six geophysical surveyed lines: (a) Line 1, (b) Line 2,  
 318 (c) Line 3, (d) Line 4, (e) Line 5, and (f) Line 6. Resistivity values increase from brown to green on the  
 319 color scale.

320 **2.3 Permeability estimation framework**

321 **2.3.1 Laboratory-based permeability determination from borehole core samples**

322 Permeability is a key hydrogeological parameter that quantifies the ability of porous media, such  
 323 as rock or sediment, to transmit fluids. It governs subsurface fluid flow and plays a central role in  
 324 groundwater studies (Allègre et al., 2016; Fiandaca et al., 2018; Mudunuru et al., 2022;  
 325 Esmailpour et al., 2023; Carbillet et al., 2024). Permeability reflects how easily fluids move  
 326 through pore networks or fractures and is typically measured via pumping tests or core analysis,  
 327 methods that are costly and logistically intensive. It is influenced by porosity, lithology,  
 328 saturation, structural features (e.g., faults, joints), and diagenetic processes (Dewandel et al.,  
 329 2006; Yan et al., 2024).

330 In the present work, initial  $k$  data from the Jinji region were limited to six boreholes. To  
331 strengthen the dataset, 116 lab tests were conducted on core samples from three main lithologies,  
332 sandstone (31), hornstone (23), and granite (62), recovered from depths up to 200 m. These data  
333 help delineate vertical  $k$  trends and refine the region's hydrogeological model. Core recovery  
334 employed a wireline rotary system with triple-tube barrels to preserve sample integrity (ISRM,  
335 2015). Samples were vacuum-sealed and stored under controlled humidity to retain in-situ  
336 moisture and fracture structure. Prior to testing, cores were trimmed to standard 50 mm ×  
337 100 mm cylinders and screened for visible defects. Two laboratory methods were used based on  
338  $k$  range. The steady-state flow test with ASTM D5084-21 guidelines (ASTM, 2021) was applied  
339 to higher- $k$  sandstone. A constant hydraulic gradient was applied under fully saturated  
340 conditions, and the corresponding volumetric flow rate was recorded. Permeability was  
341 determined through the application of Darcy's Law:

$$342 \quad k = \frac{Q \cdot \mu \cdot L}{A \cdot \Delta P} \quad (1)$$

343 where  $\Delta P$  shows the pressure differential applied across the sample (Pa),  $A$  represents the cross-  
344 sectional area (m<sup>2</sup>),  $L$  indicates the length of the sample (m),  $\mu$  shows the dynamic viscosity of  
345 the fluid (Pa·s), and  $Q$  denotes the volumetric flow rate (m<sup>3</sup>/s).

346 For low- $k$  hornstone and granite, the pulse decay method (Brace et al., 1968) was used. A  
347 brief pressure pulse was applied, and pressure decay was monitored under confining stresses up  
348 to 30 MPa to simulate in-situ conditions and assess stress-dependent  $k$  behavior. Tests were  
349 conducted under both dry and saturated conditions to evaluate moisture sensitivity. Replicate  
350 measurements ensured data reliability, and statistical analyses assessed intra- and inter-lithology  
351 variability. Results revealed that granite had the lowest  $k$  due to its dense crystalline structure,

352 while hornstone showed intermediate values, likely due to localized fracturing. Sandstone  
353 exhibited the highest  $k$ , particularly at greater depths, confirming its role as the primary aquifer  
354 unit in the region.

### 355 2.3.2 Permeability-resistivity relationship: Archie's law and the role of Kozeny–Carman

356 Numerous foundational studies have linked electrical resistivity to hydraulic properties like  $k$ . A  
357 prominent example is the Archie equation (Archie, 1942), which relates resistivity to porosity  
358 and water saturation in clean, saturated sediments. However, its assumption of clay-free  
359 conditions limits its applicability in complex or clay-rich lithologies. (Waxman and Smits, 1968;  
360 Glover, 2015). ~~The Kozeny Carman equation is another widely accepted model that links  
361 permeability to porosity and specific surface area (Bear, 1972; Carman, 1956). While it does not  
362 directly involve resistivity, it is often used alongside petrophysical models to interpret  
363 hydrogeological characteristics based on geophysical data (Paterson & Wong, 2005; Clennell,  
364 1997).~~

365 ~~Archie's law (Archie, 1942) relates the bulk electrical resistivity of a fully saturated porous  
366 medium to its porosity and fluid resistivity.~~ It is commonly expressed as:

$$367 \rho b = a \cdot \rho f \cdot \phi^{-m} \quad (2)$$

368 In this equation,  $\phi$  represents porosity,  $\rho f$  indicates fluid resistivity,  $\rho b$  denotes bulk resistivity,  
369 and  $a$  and  $m$  are empirical constants. Although Archie's law does not directly yield  $k$ , porosity  
370 serves as a useful proxy due to its strong influence on fluid movement. As such, the resistivity–  
371 porosity relationship can be leveraged to infer  $k$  indirectly, especially when supplemented with  
372 additional petrophysical frameworks (Binley et al., 2005; Revil & Cathles, 1999).

Formatted: Indent: First line: 0", Space  
Before: Auto

373 The Kozeny–Carman equation establishes a theoretical relationship between permeability  
374 ( $k$ ) and porosity ( $\phi$ ), expressed as follows:

$$375 \quad k = \frac{C \cdot \phi^3}{(1 - \phi)^2 \cdot S^2} \quad (3)$$

376 In this equation,  $k$  denotes permeability,  $\phi$  represents porosity,  $S$  is the specific surface area, and  
377  $C$  is a structural constant reflecting pore geometry and tortuosity. The Kozeny–Carman equation,  
378 though not used explicitly in this study, provides a widely accepted theoretical foundation that  
379 connects  $k$  to porosity and specific surface area (Carman, 1956; Bear, 1972). While it does not  
380 incorporate resistivity directly, this model is often used in hydrogeophysical studies to support  
381 the interpretation of petrophysical relationships that bridge electrical and hydraulic properties  
382 (Chapuis and Aubertin, 2003). Its relevance lies in the broader theoretical justification for using  
383 porosity, derived or inferred from resistivity, as a predictor of  $k$ . The application of this equation  
384 alongside Archie’s law facilitates the development of empirical or semi-empirical models that  
385 connect electrical resistivity to  $k$  (Jiang et al., 2014; Jardani et al., 2007; Glover, 2009; Yan et al.,  
386 2024).

Formatted: Font: Italic

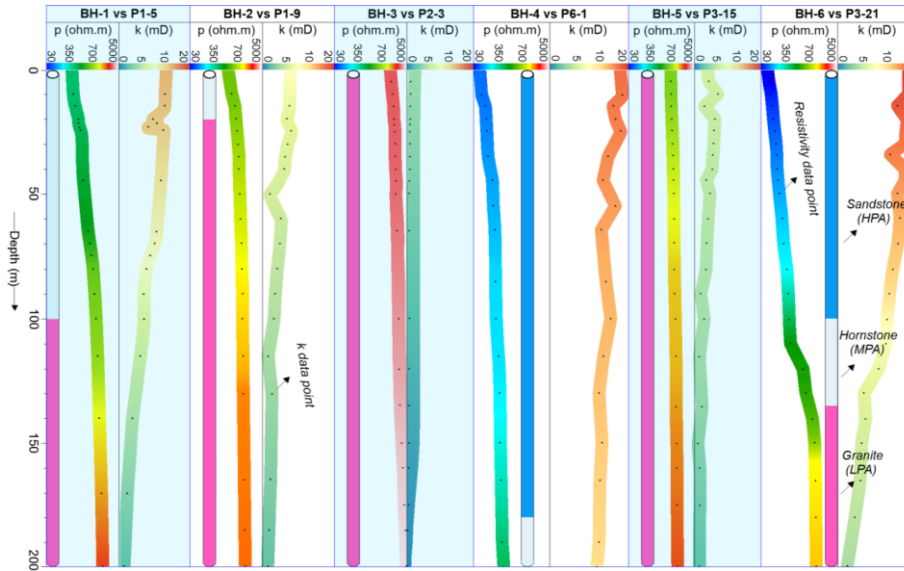
Formatted: Font: Italic

387 However, direct application of these equations to complex geological environments, such  
388 as fractured granite, sandstone, and hornstone, remains limited due to heterogeneities in mineral  
389 composition, pore connectivity, and structural anisotropy. To mitigate such constraints, our  
390 approach empirically develops a localized, site-calibrated correlation involving  $k$  and resistivity,  
391 grounded in co-located deep borehole and CSAMT data. This empirical link supports high-  
392 resolution spatial modeling of  $k$  in both 2D and 3D for the Jinji area, offering enhanced insight  
393 into subsurface hydrogeological conditions where traditional models may not be applicable.

### 394 2.3.3 Spatial permeability modeling from CSAMT data

395 To estimate permeability across the entire study area, we implemented a multi-stage approach  
396 integrating borehole core analysis with CSAMT-derived resistivity data. In the first stage, a total  
397 of 116 laboratory-based  $k$  measurements were acquired using 6 drilling tests (from BH-1 to BH-6)  
398 with 0–200 m depth (Fig. 4). The  $k$  measurements were obtained from intact rock core samples  
399 representing three principal lithologies: granite, hornstone, and sandstone.

400 In the second stage, each of the 116 borehole-derived  $k$  values was empirically correlated  
401 with corresponding resistivity values extracted from CSAMT soundings co-located with the  
402 borehole sites. The spatial correspondence between boreholes and CSAMT sounding points was  
403 carefully matched (Fig. 4). For example: P1-5 represents the fifth CSAMT sounding at 200 m  
404 along survey line 1 near borehole BH-1; P1-9 corresponds to the ninth sounding at 400 m on line  
405 1 near borehole BH-2; P2-3 denotes the third sounding at 100 m along line 2 near BH-3; P6-1  
406 indicates the first sounding at 0 m on line 6 adjacent to BH-4; P3-15 and P3-21 represent the  
407 fifteenth (700 m) and twenty-first (1000 m) soundings along line 3, near boreholes BH-5 and  
408 BH-6, respectively.



409

410 **Fig. 4.** Comparison of 116 CSAMT-based resistivity ( $\rho$ ) data points with corresponding drilling-based  
 411 permeability ( $k$ ) values at depths of 0–200 m across six borehole locations (BH-1 to BH-6). The data were  
 412 used to evaluate high potential aquifers (HPA) in sandstone, medium potential aquifers (MPA) in  
 413 hornstone, and low potential aquifers (LPA) in granite. Each dot represents a resistivity or permeability  
 414 data point. Sounding labels indicate specific CSAMT locations: P1-5 (5<sup>th</sup> point on line 1), P1-9 (9<sup>th</sup> on  
 415 line 1), P2-3 (3<sup>rd</sup> on line 2), P6-1 (1<sup>st</sup> on line 6), and P3-15 and P3-21 (15<sup>th</sup> and 21<sup>st</sup> on line 3.)

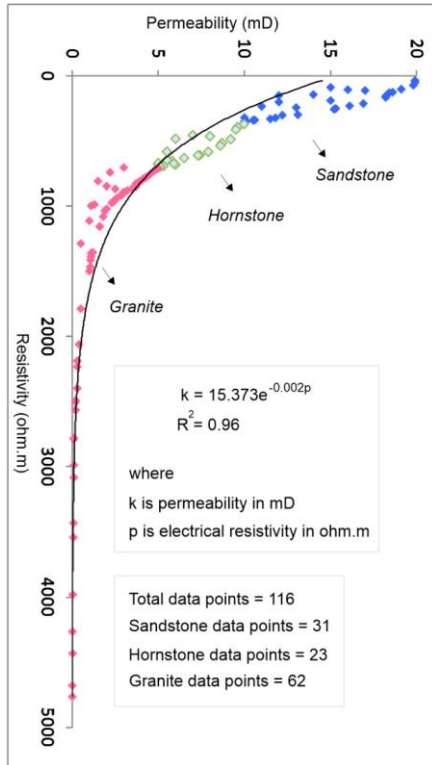
416 In the third stage, all 116 paired measurements of permeability ( $k$ ) and resistivity ( $\rho$ )  
 417 were utilized to develop an empirical model. An exponential relationship was derived between  
 418 permeability ( $k$  in millidarcies or mD) and electrical resistivity ( $\rho$  in  $\Omega$ m), expressed as follows  
 419 (Fig. 5):

420

$$k = 15.373(e)^{-0.002(\rho)} \quad (43)$$

421 This site-specific empirical model was then applied to the entire suite of CSAMT resistivity data  
422 collected along six survey profiles to estimate spatial variations in  $k$  across the broader study area.  
423 Using this relationship, we generated predictive 2D and 3D  $k$  models that capture the hydraulic  
424 behavior of three major lithological units: low potential aquifer (LPA): associated with low-  
425 permeability granite, medium potential aquifer (MPA): hosted within fractured hornstone  
426 (hornfels), high potential aquifer (HPA): corresponding to more porous sandstone units.

427 These models provide a depth-resolved assessment of subsurface  $k$  reaching depths of up  
428 to 1300 m below the surface. Final 2D and 3D spatial visualizations were developed by SKUA-  
429 GOCAD and Geosoft Oasis montaj modeling software (Webring, 1981; Mira Geoscience Ltd.,  
430 1999; Hasan et al., 2024), enabling the visualization of  $k$  distributions across all six CSAMT  
431 profiles and improving hydrogeological characterization in structurally complex hard rock terrain.



432

433 **Fig. 5.** Empirical relationship derived from 116 data points comparing CSAMT-based resistivity and  
 434 drilling-based  $k$  at depths of 0–200 m, across three lithologies: sandstone (31 data points), hornstone (23  
 435 data points), and granite (62 data points).

### 436 3 Results

#### 437 3.1 Cross-validation of geophysical and borehole parameters

438 [Table 1](#) summarizes the integrated dataset from 6 drills and 6 geophysical profiles to resolve the  
 439 spatial structure of the subsurface into three distinctive hydrogeological units, based on  
 440 variations in electrical resistivity and corresponding  $k$  values. The development of these

441 subsurface models mainly depends on borehole data, CSAMT-derived resistivity measurements,  
 442 and the regional geological framework. The stratigraphy was categorized into three primary  
 443 lithologies: sandstone, hornstone, and granite. Classification criteria were established as follows:  
 444 sandstone was defined by resistivity values below 350  $\Omega\text{m}$  and a  $k$  range of 10–20 mD;  
 445 hornstone exhibited resistivity values between 350 and 700  $\Omega\text{m}$  with a  $k$  range of 5–10 mD; and  
 446 granite was characterized by resistivity values exceeding 700  $\Omega\text{m}$  and  $k$  values ranging from 0 to  
 447 5 mD. Based on our evaluations of the subsurface hydrogeological model's aquifer potential  
 448 zones, we found that sandstone contains the high potential aquifer (HPA), hornstone contains  
 449 medium potential aquifer (MPA), and granite has low potential aquifer (LPA). Aquifers with the  
 450 largest yields or the best water-bearing capacity are indicated by sandstone, whereas aquifers  
 451 with the lowest yields or the worst water-bearing capacities are denoted by granite. Groundwater  
 452 development is best facilitated by sandstone in the study area, whereas groundwater extraction is  
 453 most hindered by granite.

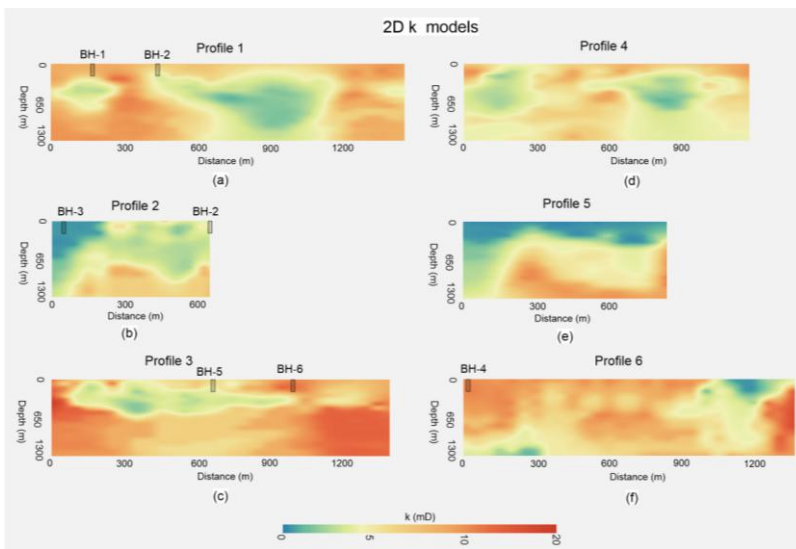
454 **Table 1**

455 Integrating distinct ranges of electrical resistivity and  $k$  enables a comprehensive assessment of  
 456 groundwater potential across various hard rock types

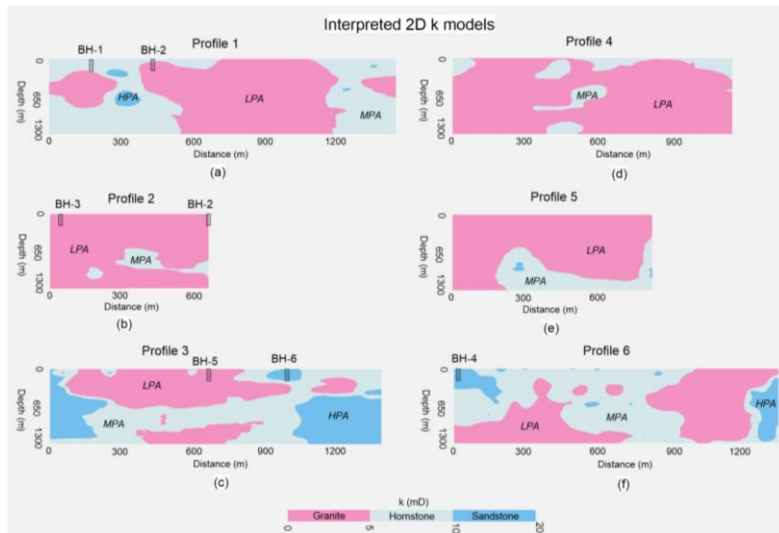
Resistivity ( $\Omega\text{m}$ )	$k$ (mD)	Type of rock	Aquifer potential
< 350	10–20	Sandstone	High potential aquifer (HPA)
350–700	5–10	Hornstone	Medium potential aquifer (MPA)
>700	0–5	Granite	Low potential aquifer (LPA)

457 **3.2 2D groundwater assessments**

458 Using geophysical-borehole correlation as its basis, Eq. (43) efficiently converts 2D CSAMT  
459 models (Fig. 3) into 2D  $k$  models (Fig. 6). The interpreted 2D  $k$  models shown in Fig. 7, in  
460 comparison with the limited borehole experiments, allow for a comprehensive assessment of the  
461 groundwater resources in hard rock across the whole research area, from 0 to 1300 m deep.



462  
463 **Fig. 6.** The predicted 2D  $k$  models along six geophysical surveyed lines: (a) Line 1, (b) Line 2, (c) Line 3,  
464 (d) Line 4, (e) Line 5, and (f) Line 6.  $k$  values increase from blue to red on the color scale.

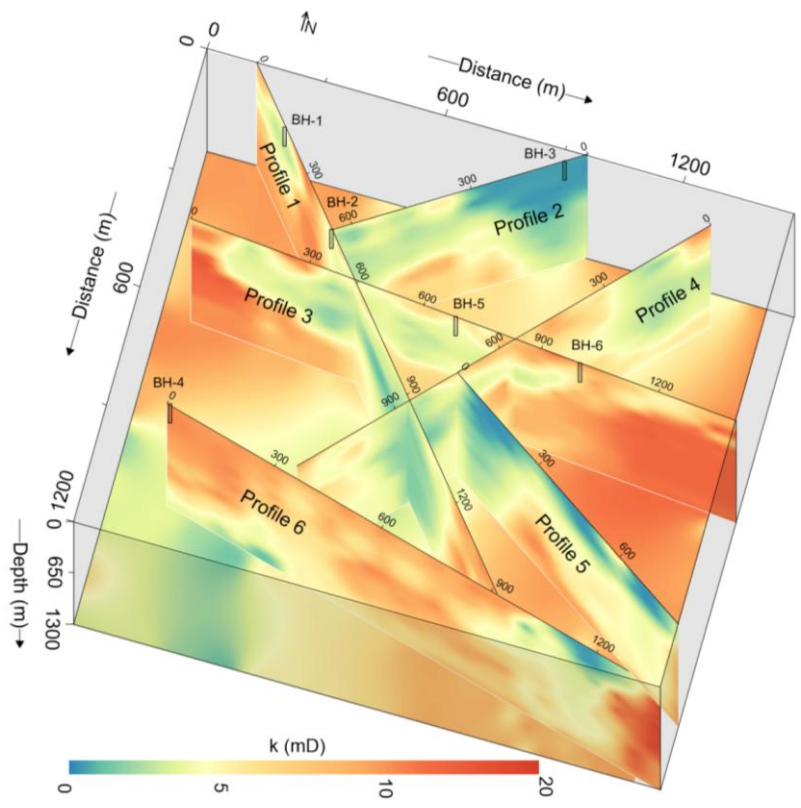


465

466 **Fig. 7.** The interpretation of the predicted 2D  $k$  models along six geophysical surveyed lines: (a) Line 1,  
 467 (b) Line 2, (c) Line 3, (d) Line 4, (e) Line 5, and (f) Line 6. Sandstone is represented in blue, hornstone in  
 468 light blue, and granite in pink

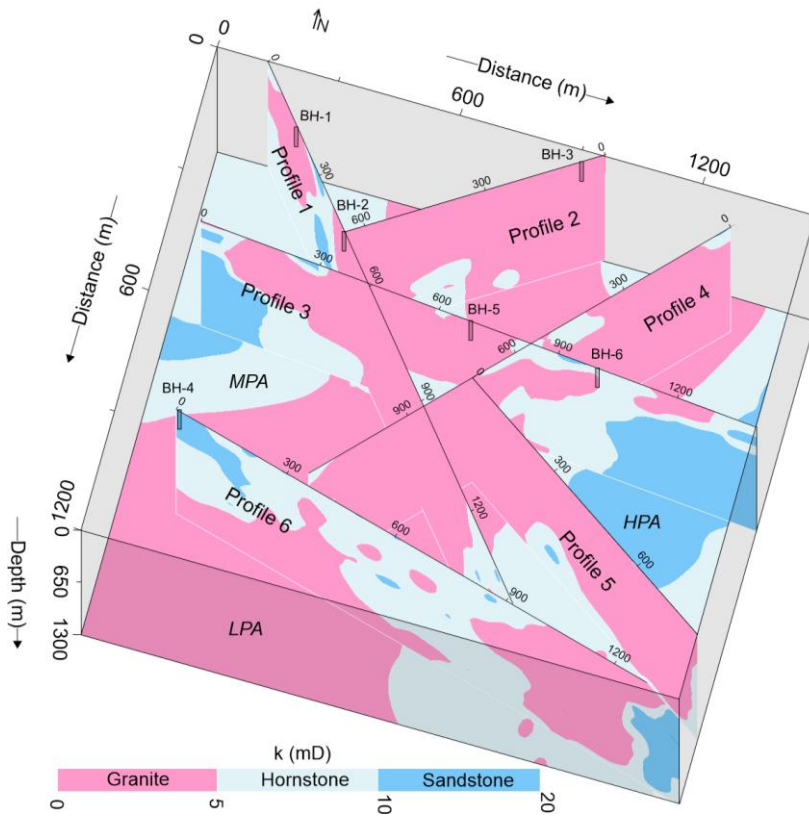
469 The integrated 2D  $k$  models (Fig. 8) and their interpretations (Fig. 9) provide a detailed  
 470 evaluation of groundwater potential across complex geological settings of sandstone, hornstone,  
 471 and granite. Profile 1 reveals a high-potential sandstone aquifer (85–305 m thick) between 245–  
 472 380 m distance at 205–400 m depth. Medium-potential hornstone aquifers are found from 0–525  
 473 m and 1185–1445 m distance down to 1300 m. Low-potential granite aquifers appear at 0–285 m  
 474 (290–790 m depth), 385–1185 m (full depth), and 1305–1450 m (390–745 m depth). Profile 2  
 475 shows a medium-potential hornstone aquifer with 140–380 m thickness (490–1105 m depth)  
 476 between 145–215 m and 290–645 m distance. No high-potential sandstone aquifers are present.  
 477 Granite dominates (0–700 m distance, 0–1300 m depth) the profile with low yield except in  
 478 hornstone zones. Profile 3 contains both high-potential sandstone (0–250 m, 905–1065 m, and

479 1040–1390 m distances at respective depths of 0–1190, 0–205, and 490–1305 m) and medium-  
480 potential hornstone aquifers (full depth with 0–1400 m distance) across the entire surveyed line.  
481 Granite aquifers are assessed at 80–1015 m (0–590 m depth), 395–845 m (915–1300 m depth),  
482 and 1100–1300 m (200–500 m depth). Profile 4 features medium-potential hornstone at 0–105 m  
483 (0–340 m depth), 340–645 m (0 to 1300 m depth), 595–790 m (0–300 m depth), and 1015–1145  
484 m (0–345 m depth). No high-potential sandstone is observed. Granite aquifers of low potential  
485 dominate (0–1145 m distance between 0–1300 m depth), except in hornstone zones. Profile 5  
486 shows medium-potential hornstone (190–845 m distance, 390–1300 m depth) and two small  
487 high-yield sandstone patches (290 m at 790–960 m depth and 815 m at 1045–1135 m depth).  
488 Low-potential granite appears at distance 0–190 m (0–1300 m depth) and 790–815 m (0–1025 m  
489 depth). Profile 6 includes high-potential sandstone zones at 0–190 m (0–490 m depth) and 1245–  
490 1345 m (215–1225 m depth). Low-potential granite is present at 0–690 m (390–1300 m depth)  
491 and 790–1360 m (0–1190 m depth), while hornstone with medium potential dominates the  
492 remainder. Overall, the southeastern and northwestern zones host abundant medium- to high-  
493 potential aquifers, while central regions show limited or poor groundwater prospects.



494

495 **Fig. 8.** The integrated 2D  $k$  models derived from the incorporation of geophysical and drilling data, with  $k$   
 496 represented on a color bar spanning from green to red



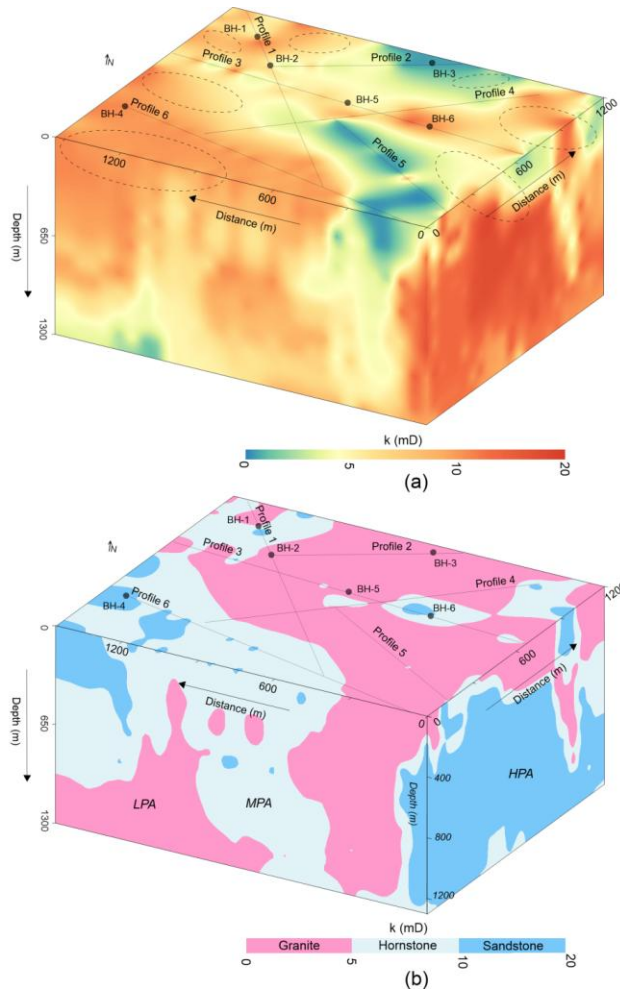
497

498 **Fig. 9** Analysis of 2D  $k$  models, based on defined  $k$  ranges, for three groundwater potential aquifers: low  
 499 potential aquifer (LPA), medium potential aquifer (MPA), and high potential aquifer (HPA),  
 500 corresponding to the granite, hornstone, and sandstone formations, respectively

501 **3.3 3D groundwater assessments**

502 The 3D  $k$  (outer view) visualization (Fig. 10a, b) provides a comprehensive assessment of the  
 503 water-bearing capacity of the rock mass. Low-potential granite aquifers are found at the surface  
 504 along: line 1 (85–215 m, 385–1175 m), line 2 (0–655 m), line 3 (0–45 m, 95–175 m, 265–585 m,  
 505 605–845 m, 1145–1315 m), line 4 (90–390 m, 490–615 m, 745–1115 m), line 5 (0–815 m), and

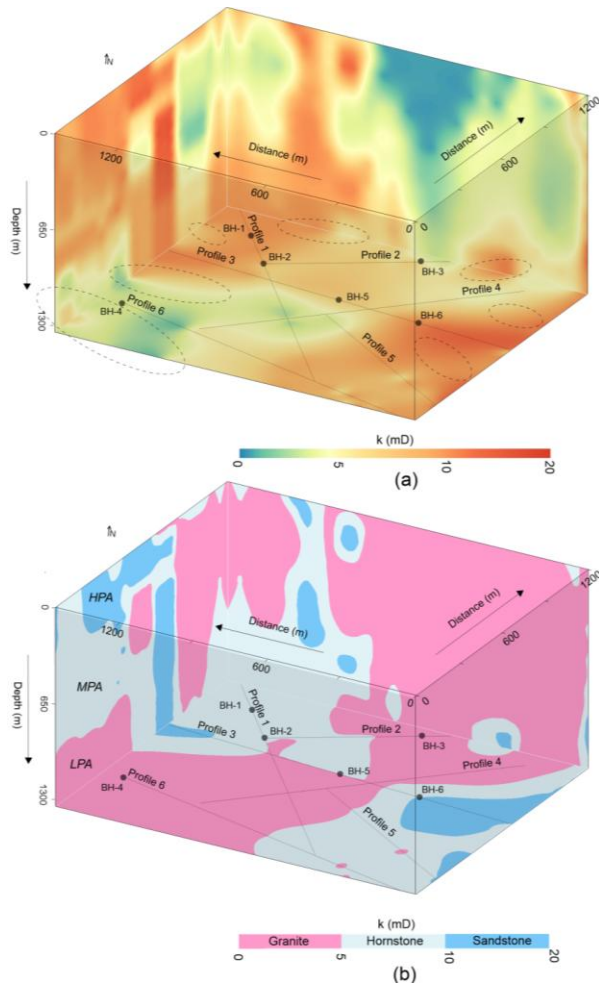
506 line 6 (1045–1345 m). Medium-potential hornstone aquifers appear along: line 1 (0–95 m, 190–  
507 260 m, 295–415 m, 1185–1425 m), line 3 (40–105 m, 215–275 m, 580–605 m, 850–910 m,  
508 1010–1155 m, 1310–1410 m), line 4 (45–90 m, 390–490 m, 590–685 m, 1115–1185 m), and line  
509 6 (90–190 m, 215–275 m, 315–485 m, 505–605 m, 635–1045 m). High-potential sandstone  
510 aquifers are identified in: line 1 (265–310 m), line 3 (235–255 m, 915–1010 m), line 4 (0–45 m),  
511 and line 6 (0–90 m, 210–225 m, 275–305 m, 515–525 m, 605–635 m). Overall, [Fig. 10 \(a, b\)](#)  
512 shows that higher-yield aquifers are mainly concentrated in the southern portion of the  
513 investigated site.



514

515 **Fig. 10.** The 3D  $k$  models (CSAMT-based), with  $k$  shown on a color scale increasing from green to red,  
 516 correspond to three groundwater potential aquifers: low potential aquifer (LPA), medium potential aquifer  
 517 (MPA), and high potential aquifer (HPA), associated with three geological strata: granite, hornstone, and  
 518 sandstone, respectively. The uncertainty contours (highlighted by areas with black dots) indicate zones of  
 519 reduced confidence in  $k$  estimation. (a) The exterior visualization of the 3D  $k$  model, and (b) The analysis  
 520 of the 3D  $k$  model from an external perspective

521            Fig. 11 (a, b) shows a 3D internal view of aquifer potential at 1300 m depth. Low-yield  
522 granite aquifers are identified along: surveyed line 1 (515–1215 m), line 2 (0–290 m), line 3  
523 (390–690 m), line 4 (0–1145 m), line 5 (0–195 m, 565–595 m), and line 6 (0–690 m, 1075–1115  
524 m). Medium-potential hornstone aquifers are found along: profile 1 (0–540 m, 1215–1445 m),  
525 profile 2 (295–675 m), profile 3 (175–395 m, 445–815 m, 915–1035 m), profile 5 (205–565 m,  
526 610–815 m), profile 6 (685–1080 m, 1110–1355 m). High-potential sandstone aquifers appear  
527 along: profile 3 (0–205 m, 1010–1400 m) and profile 5 (810–815 m). Overall, medium to high  
528 potential aquifers are mainly distributed in the southeastern and northwestern regions, while  
529 central areas are dominated by low-yield granite. The aerial 3D  $k$  model enhances visualization  
530 of aquifer distribution, supporting accurate groundwater assessment.



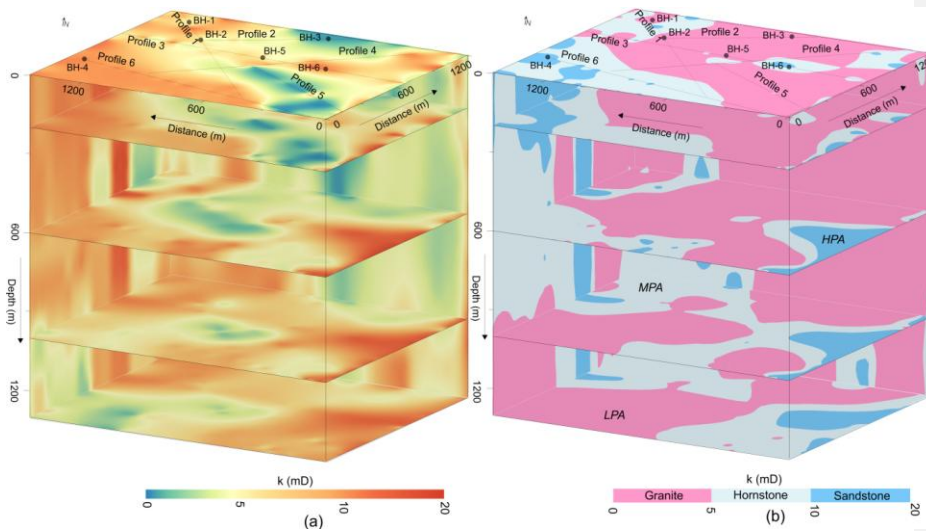
531

532 **Fig. 11.** The 3D  $k$  models (CSAMT-based), with  $k$  represented on a color scale ranging from green, to red,  
 533 illustrate three groundwater potential aquifers: low potential aquifer (LPA), medium potential aquifer  
 534 (MPA), and high potential aquifer (HPA), associated with three geological strata: granite, hornstone, and  
 535 sandstone-, respectively, respectively. The uncertainty contours (highlighted by areas with black dots)  
 536 indicate zones of reduced confidence in  $k$  estimation. (a) The interior visualization of the 3D  $k$  model, and  
 537 (b) The analysis of the 3D (internal perspective)  $k$  model

538 **3.4 Depth-wise groundwater assessments**

539           Due to limited borehole data, direct estimation of  $k$  below 200 m is not feasible.  
540           However, by integrating borehole and CSAMT data,  $k$  values could be reliably estimated down  
541           to 1300 m. This approach enabled efficient and detailed evaluation of hard rock aquifers using  
542           both 2D and 3D models (Fig. 12), with  $k$  values extracted at depths of 0, 200, 600, 1000, and  
543           1300 m. At 1300 m, over 42% of the subsurface in the southwest and northeast comprised low-  
544           yield granite. Hornstone accounted for 40% (medium yield) near granite zones in the northwest  
545           and southeast, while high-yield sandstone made up 18% in the east. At 1000 m, sandstone (15%)  
546           was concentrated in the southeast (high yield), hornstone (38%) in the southeast and northwest  
547           (medium yield), and granite (47%) dominated the central and boundary zones (low yield). At  
548           600 m, the subsurface was 55% granite (central and northern zones, low yield), 32% hornstone  
549           (western region, medium yield), and 13% sandstone (southeast, high yield). At 200 m, granite  
550           dominated 64% of the center and north (low yield), hornstone made up 26% in the south  
551           (medium yield), and sandstone (10%) in the west was associated with high yield. At 0 m, 73% of  
552           the central area comprised low-yield granite, 20% of the southwest was hornstone (medium  
553           yield), and 7% sandstone (high yield) was concentrated in the southwest.

554           Overall, Fig. 12 shows a decrease in low-yield granite thickness with depth. Groundwater  
555           potential is lowest around 600–700 m depth, while deeper zones (>700 m) in the northwest,  
556           southeast, and southwest show more favorable aquifer conditions.



557

558 **Fig. 12.** (a) Geophysical  $k$  imaging at depths of 0, 200, 600, 1000, and 1300 m, with  $k$  shown on a color  
 559 scale increasing from green to red. (b) Evaluation of CSAMT-derived  $k$  values (based on defined  $k$  ranges)  
 560 at various depths for different aquifer types: low potential aquifer (LPA) in granite, medium potential  
 561 aquifer (MPA) in hornstone, and high potential aquifer (HPA) in sandstone

### 562 3.5 Validation of predicted vs. measured permeability

563 Groundwater evaluation was greatly improved by systematic CSAMT-based  $k$  estimation. As  
 564 shown in Figs. 6–12, granite dominates the central, northeastern, and southwestern zones;  
 565 hornstone occurs mainly in the southeast, west, and northwest; and sandstone is prevalent in the  
 566 east. Borehole-based assessments are limited by inconsistent subsurface mapping. While  $k$  values  
 567 align near 200 m depth, broader extrapolation remains uncertain, highlighting the limitations of  
 568 sparse drilling in complex geology.

569 To clarify the basis of the percentage matching values, the following explicit equation  
570 was used to quantify the agreement between CSAMT-derived  $k$  values and borehole-based  $k$   
571 estimates:

Formatted: Font: Italic

Formatted: Font: Italic

572 
$$\text{Percentage Matching} = \left( \frac{N_s}{N_l} \right) \times 100 \quad (4)$$

573 Here,  $N_s$  represents the smaller of the two  $k$  values, either from the CSAMT model or borehole  
574 data, at a given depth, while  $N_l$  is the larger. This ratio offers a normalized agreement metric,  
575 where 100% indicates a perfect match and lower values reflect greater divergence. Comparisons  
576 were made at multiple depth intervals across six calibration boreholes. Table 2 summarizes the  
577 percentage agreement for 18 selected data points (out of 116) between measured and predicted  $k$   
578 values. Agreement was calculated at matched depth intervals for each borehole–sounding pair  
579 using Eq. (3). For example, BH-1 and P1-5 show 73%, 63%, and 100% agreement at 10, 40, and  
580 170 m depth. BH-2 and P1-9 exhibit 80%, 77%, and 85% agreement at 20, 60, and 185 m depth.  
581 Other pairings, such as BH-3 with P2-3, show lower agreement (67%, 40%, 30%) at 10, 85 and  
582 200 m depth, while BH-5 and P3-15 yield high matches of 80%, 94%, and 85% at 30, 135, and  
583 200 m depth, and BH-6 and P3-21 produce matches of 61%, 74%, and 71% at 45, 165, and 180  
584 m depths, respectively.

Formatted: Font: Italic

585 Overall, the results indicate strong consistency between observed and predicted values,  
586 with discrepancies likely due to local heterogeneity or measurement uncertainty. Even at lower  
587 %percent match, both methods often classify the site into the same aquifer potential zone,  
588 supporting the robustness of the CSAMT-based approach for regional groundwater assessment.

589 **Table 2**

590 Percentage match and deviation between the measured  $k$  and the predicted  $k$  for 18 selected data points  
 591 out of the total 116

CSAMT data points (selected)			Drilling data			%Matching	Difference
CSAMT sounding number	Resistivity ( $\Omega\text{m}$ )	Predicted $k'$ (mD) using Eq. (43)	Borehole name	Depth (m)	Measured $k$ (mD)	$k'$ vs $k$	between $k'$ and $k$
P1-5	392	7.0	BH-1	10	9.6	73	2.6
P1-5	515	5.5	BH-1	40	8.7	63	3.2
P1-5	1080	1.8	BH-1	170	1.8	100	0.0
P1-9	669	4.0	BH-2	20	5.0	80	1.0
P1-9	863	2.7	BH-2	60	3.5	77	0.8
P1-9	1354	1.02	BH-2	185	1.2	85	0.18
P2-3	2187	0.2	BH-3	10	0.3	67	0.1
P2-3	2988	0.04	BH-3	85	0.1	40	0.06
P2-3	4765	0.003	BH-3	200	0.01	30	0.007
P6-1	50	13.9	BH-4	15	19.9	70	6.0
P6-1	200	10.3	BH-4	100	12.0	86	1.7
P6-1	348	7.7	BH-4	180	9.9	78	2.2
P3-15	792	3.3	BH-5	30	4.1	80	0.8
P3-15	1157	1.5	BH-5	135	1.6	94	0.1
P3-15	1412	0.91	BH-5	200	1.07	85	0.16
P3-21	165	11.1	BH-6	45	18.2	61	7.1
P3-21	708	3.7	BH-6	165	5.0	74	1.3
P3-21	846	2.8	BH-6	180	2.0	71	0.8

592

593 **4 Discussion**

594 **4.1 Scalable geophysical approach for deep groundwater modeling**

595 The integration of geophysics into groundwater studies provides an efficient and scalable  
596 substitute for borehole-based methods, especially in deep and geologically complex terrains.  
597 While boreholes provide direct  $k$  data, their use is limited by cost, logistics, and sparse coverage.  
598 Our study presents a robust framework for 2D and 3D  $k$  modeling beyond 1 km depth by  
599 integrating CSAMT with borehole data in a lithologically diverse setting. This approach  
600 addresses key challenges in areas with limited surface water and low- $k$  granite near the surface,  
601 revealing deeper fractured zones with higher groundwater potential in granite, hornstone, and  
602 sandstone. These deep aquifer insights support China's national water security strategies and  
603 inform sustainable groundwater management under climate stress.

604 **4.2 Ensuring data quality and model reliability**

605 To minimize uncertainty and enhance accuracy, we implemented a rigorous workflow  
606 throughout data acquisition, processing, inversion, and modeling. For CSAMT, this included  
607 careful survey planning, optimized electrode configurations, and the application of advanced  
608 filtering and static shift corrections. Inversion was guided by multidimensional modeling  
609 constrained by borehole-derived a priori information, improving resolution and mitigating non-  
610 uniqueness. Permeability measurements were obtained under controlled laboratory conditions  
611 using high-quality, undisturbed core samples from six boreholes, reducing discrepancies between  
612 laboratory and field scales. These measures, together with integrated lithological data, enabled  
613 the development of a robust  $k$  model suitable for reliable groundwater assessment across the  
614 study area.

Formatted: Font color: Auto

615 **4.3 Comparative advantages of CSAMT for deep hard rock aquifer characterization**  
616 CSAMT, developed in the 1970s, remains uniquely valuable for deep subsurface exploration,  
617 particularly in resistive and fractured hard rock environments. Its ability to image at  
618 intermediate-to-deep depths (hundreds to over a thousand meters) with relatively high resolution  
619 and controlled signal strength enhances its ability to delineate lithological contacts and fluid-  
620 bearing formations with precision and where other resistivity methods (VES and ERT) may fall  
621 short. While other electromagnetic methods such as MT and TDEM are also capable of probing  
622 deep subsurface structures, achieving comparable results with these methods in similarly  
623 complex hard rock settings presents notable challenges. MT, which relies on natural variations in  
624 electromagnetic fields, can reach even greater depths than CSAMT and has been successfully  
625 applied in regional-scale hydrogeological investigations, such as identifying deep groundwater  
626 circulation paths in mountain systems (Jiang et al., 2014) and tracing flow systems that recharge  
627 lowland aquifers (Gonzalez-Duque et al., 2024). However, MT's lower resolution in the upper  
628 crust and dependency on natural field conditions often limit its effectiveness in detailed, site-  
629 specific  $k$  modeling, particularly when borehole calibration is sparse. Similarly, TDEM is widely  
630 used for near-surface to intermediate-depth investigations and offers rapid deployment, but its  
631 signal strength and resolution tend to decrease in highly resistive formations, making it less  
632 suitable for imaging deep, fractured zones in hard rock. Therefore, while MT and TDEM are  
633 powerful methods for broad-scale groundwater assessment, they are less suited to the high-  
634 resolution, volumetric modeling of  $k$  in varied lithologies beyond 1km depth. In contrast,  
635 CSAMT's controlled-source design, moderate-to-deep depth penetration, and strong signal-to-  
636 noise ratio in resistive environments make it better aligned with the goals of this study. The  
637 approach bridges the gap between large-scale geophysical surveys (e.g., MT or TDEM) and

Formatted: Font: Not Bold, Italic

Formatted: Font: Not Bold, Italic

638 localized drilling, enabling spatially continuous 2D and 3D hydrogeophysical models essential  
639 for evaluating deep aquifer potential. While MT or TDEM may complement such studies at  
640 regional scales, achieving this level of resolution and lithological detail in a hard rock context  
641 currently remains more feasible with CSAMT.

#### 642 **4.4 Calibrated resistivity thresholds for lithological and hydraulic discrimination**

643 We developed a robust empirical relationship between resistivity and  $k$  using 116 co-located data  
644 pairs, 62 from granite, 31 from sandstone, and 23 from hornstone, spanning 35–4,765  $\Omega\text{m}$  and  
645 0.01–19.9 mD, respectively. The strong correlation ( $R^2 = 0.96$ ) ensures reliable  $k$  prediction and  
646 minimizes lithological bias. The lithological classification derived from the resistivity–  
647 permeability relationship in this study is both geologically plausible and empirically supported  
648 by borehole data and field observations. Specifically, granite showed high resistivity ( $>700 \Omega\text{m}$ )  
649 and low  $k$  (0–5 mD), hornstone had intermediate resistivity (350–700  $\Omega\text{m}$ ) and moderate  $k$  (5–  
650 10 mD), and sandstone was marked by low resistivity ( $<350 \Omega\text{m}$ ) and higher  $k$  (10–20 mD).

651 These ranges align with the distinct hydrogeological behaviors of each lithology under the site-  
652 specific structural and mineralogical conditions. The resistivity thresholds were selected through  
653 an integrated approach combining lithological logs from boreholes, established empirical  
654 resistivity values reported in the literature, and the geoelectrical contrasts identified in CSAMT  
655 profiles. For instance, the high resistivity of granite reflects its dense, low-porosity matrix and  
656 limited fluid content, whereas the lower resistivity of sandstone and hornstone corresponds to  
657 increased pore connectivity and higher saturation, often enhanced by structural features or  
658 thermal alteration. To ensure robust classification, the resistivity thresholds were calibrated using  
659 co-located borehole observations from multiple calibration sites and iteratively refined to  
660 maximize agreement between observed lithology and the modeled resistivity–permeability

Formatted: Font: Not Bold, Italic

661 domains. While we acknowledge that resistivity can vary within a given lithology due to  
662 localized factors such as fluid saturation, mineral alteration, or fracture density, sensitivity  
663 analyses indicated that moderate adjustments to the threshold values had minimal impact on the  
664 overall lithological classification or the interpretation of  $k$  trends. This suggests that the chosen  
665 thresholds are well-suited to the structurally complex Jinji area. Nevertheless, we emphasize that  
666 these resistivity–permeability associations are localized and should be recalibrated to account for  
667 site-specific conditions before use elsewhere. Although site-specific, the approach demonstrates  
668 how minimal calibration data can support high-resolution 2D/3D  $k$  modeling in data-scarce  
669 settings. Future studies could benefit from probabilistic classification schemes or machine  
670 learning approaches to further refine lithological mapping in geologically heterogeneous terrains.

Formatted: Font: Not Bold, Italic

671 **4.5 Impact of lithological and measurement variability on the resistivity–permeability**  
672 **relationship**

Formatted: Font: (Default) Times New Roman, 12 pt, Font color: Auto

Formatted: Font: (Default) Times New Roman, 12 pt, Font color: Auto

673 The fitted relationship between resistivity and  $k$ , as illustrated in Fig. 5, is shaped by several  
674 factors, including the geological setting, lithological heterogeneity, data distribution, and the  
675 accuracy of both measurements. The broad dynamic range in our dataset provides a strong basis  
676 for identifying trends across the three dominant lithologies: sandstone, granite, and hornstone.  
677 This broad range is especially beneficial for resolving low- $k$  formations such as granite, where  $k$   
678 remains uniformly low and shows minimal fluctuation. In these settings, even large shifts in  
679 resistivity translate to relatively small changes in  $k$ , resulting in a gently declining inverse  
680 relationship. In contrast, at lower resistivity values (e.g.,  $<1,000 \Omega\text{m}$ ) where  $k$  exceeds 2 mD,  
681 small resistivity shifts result in larger changes in  $k$ , leading to a more scattered and nonlinear  
682 correlation. This pattern is geologically realistic and reflects the inherent variability of fractured  
683 and porous zones in complex lithologies.

684 **4.6 Model validation and predictive reliability**

Formatted: Indent: First line: 0"

685 Matching between measured and predicted permeability ( $k$  vs.  $k'$ ) was also rigorously validated  
686 (Table 2). Among 18 selected points from boreholes, 10 showed a difference of less than 1 mD,  
687 with only two exceeding 4 mD. Despite minor deviations, all points were accurately classified by  
688 lithology. This confirms the empirical model's reliability and its utility for regional-scale  $k$   
689 prediction, even in areas lacking direct measurements. The geophysical model effectively  
690 compensates for sparse drilling data, offering a scalable and cost-effective tool for  
691 hydrogeological evaluation in hard rock terrains.

692 **4.7 Scale compatibility between CSAMT and permeability measurements**

Formatted: Font: Bold

693 Although pumping tests provide bulk estimates of  $k$ , they lack the spatial resolution needed for  
694 detailed 2D or 3D modeling. Our goal was to capture subsurface heterogeneity, which required  
695 point-specific  $k$  measurements aligned with the localized nature of geophysical-based resistivity.  
696 Core data were used in lieu of pumping tests to meet the objective. The  $k$  data derived from core  
697 samples at discrete depths provided a fine-scale match with CSAMT resistivity, improving the  
698 accuracy of the empirical  $k$ - $\rho$  (resistivity-permeability) relationship. The spatial resolution of  
699 CSAMT ( $\sim 50 \times 50$  m) closely corresponds to the scale of the core samples, ensuring  
700 compatibility between datasets and supporting reliable modeling in complex geological settings.

701 **4.8 Inflection in the resistivity-permeability relationship: a depth analogue**

702 The empirical resistivity-permeability ( $k$ - $\rho$ ) relationship developed in this study exhibits a sharp  
703 decline in  $k$  with increasing resistivity and a clear inflection near 1,000  $\Omega$ m. This mirrors classic  
704 depth-permeability ( $k$ - $z$ ) trends (e.g., Manning and Ingebritsen, 1999; Saar and Manga, 2004;  
705 Ingebritsen and Manning, 2010), where  $k$  decreases exponentially at shallow depths and follows

Formatted: Font: Not Bold, Italic

706 a power-law pattern deeper down. However, unlike those models that use depth alone, our  
707 resistivity-based approach captures additional controls such as lithology, porosity, fluid content,  
708 and fracturing, making it a more localized and physically representative proxy, especially in  
709 heterogeneous hard rock settings.

710 Depth was considered but not used as the primary variable due to strong lateral variations  
711 in resistivity and  $k$  caused by geological complexity. For instance, in the Jinji area, surface  
712 granite shows high resistivity and low  $k$ , consistent with standard crustal profiles. However,  
713 deeper hornstone and sandstone units exhibit lower resistivity and higher  $k$ , contrary to typical  
714 depth trends, likely due to localized faulting, thermal alteration, and contact metamorphism that  
715 enhance fracture connectivity. The resemblance between our  $k$ - $\rho$  curve and established  $k$ - $z$   
716 models reinforces its physical validity. The observed transition near 1,000  $\Omega$ m may reflect a shift  
717 from conductive, fractured zones to compact, resistive rock masses. While hybrid models  
718 incorporating depth may be useful in future work, our resistivity-based method provides a more  
719 reliable and site-specific approach for  $k$  estimation in structurally complex terrains.

Formatted: Font: Not Bold, Italic

#### 720 4.9 Salinity effects and limitations of deep calibration

721 The influence of factors beyond lithology, particularly groundwater salinity, on CSAMT-derived  
722 resistivity warrants consideration. Electrical resistivity is inherently sensitive to porosity, fracture  
723 density, mineral alteration, fluid saturation, and salinity. In this study,  $k$  calibration was based on  
724 core samples from 0–200 m depths across six boreholes. While this limits direct calibration at  
725 greater depths, hydrochemical data from the Geological Survey of China, spanning 800–1,000 m  
726 depth, consistently indicate fresh groundwater, suggesting salinity is not the cause of deeper low-  
727 resistivity zones. We interpret these zones, especially in sandstone and hornstone, as reflecting

Formatted: Indent: First line: 0"

Formatted: Font: Not Bold, Italic

728 high saturation and pore connectivity rather than saline fluids. This is further supported by the  
729 absence of resistivity anomalies typically associated with brackish water, and the strong  
730 alignment between resistivity,  $k$ , and lithological boundaries. However, due to the lack of salinity  
731 data below 1 km, the role of deep fluid conductivity cannot be fully ruled out, a limitation of the  
732 current study. Future work should include deep borehole sampling and in-situ fluid logging to  
733 better constrain this relationship.

Formatted: Font: Not Bold, Italic

#### 734 **4.10 Model construction and uncertainty in 3D permeability mapping**

735 The 3D  $k$  model was developed by interpolating between 2D CSAMT inversion profiles  
736 calibrated with borehole-derived  $k$  from six reference locations. Due to limitations in survey  
737 geometry and computational cost, full 3D inversion was not feasible. Instead, a geostatistical  
738 framework using ordinary kriging integrated cross-sections and applied the resistivity–  
739 permeability relationship across the volume, constrained by lithological boundaries and borehole  
740 data. While this approach provides a volumetric view of  $k$ , model reliability declines toward the  
741 edges and corners where data density is limited. Sensitivity analyses, based on variogram  
742 adjustments and comparisons of interpolation algorithms, revealed elevated uncertainty in these  
743 peripheral zones. To convey this, uncertainty contours were added to the 3D figures (Figs. 10  
744 and 11), delineating areas of reduced confidence. The model's core, where CSAMT lines  
745 intersect and borehole constraints exist, offers the highest reliability. Boundary regions should be  
746 interpreted with caution. Future work with denser CSAMT coverage or full 3D inversion would  
747 enhance model accuracy and reduce edge-related uncertainties.

Formatted: Indent: First line: 0"

Formatted: Font: Not Bold, Italic

Formatted: Font: Not Bold, Italic

Formatted: Font: Not Bold, Italic

#### 748 **4.11 Limitations of storage characterization**

749 A complete groundwater assessment requires evaluating both  $k$  and storage parameters. This  
750 study focused on delineating spatial variations in  $k$ , referred to here as “water-bearing capacity”,  
751 using CSAMT-derived resistivity calibrated with borehole data. While we emphasize  $k$ , we  
752 acknowledge that key storage parameters such as porosity, specific yield, and specific storage  
753 remain unmeasured due to the absence of deep aquifer tests and formation logs. However,  
754 geological and geophysical evidence allows for qualitative inference. Permeable units like  
755 sandstone and hornstone likely possess higher porosity due to their granular textures and fracture  
756 networks, unlike the denser granite. This is supported by groundwater level data from six  
757 boreholes and regional water table records, which indicate aquifers in fractured, low-resistivity  
758 zones. These zones align spatially with permeable features in both CSAMT/ $k$  models and  
759 borehole data. Our current interpretation focuses on relative transmissivity, not absolute storage  
760 capacity, a limitation we acknowledge. Future work should include porosity and storage  
761 measurements through deep borehole testing, in-situ logging, and hydraulic analysis to support  
762 more comprehensive aquifer characterization in complex hard rock settings.

Formatted: Indent: First line: 0"

Formatted: Font: Not Bold, Italic

#### 763 4.12 Optimizing borehole placement for CSAMT calibration

764 Borehole placement in this study was strategically guided by geological mapping, hydrological  
765 relevance, and preliminary geophysical data to ensure representative coverage of key lithologies  
766 and structures. These boreholes served both to calibrate resistivity–permeability relationships  
767 and to validate the CSAMT-derived  $k$  models. While there’s no fixed number of required  
768 boreholes, our results show that a small but well-distributed set across major lithological and  
769 structural zones yields reliable model performance. A leave-one-out validation confirmed that  
770 the model maintains coherent spatial trends, though with slightly reduced accuracy in

Formatted: Font: (Default) Times New Roman, 12 pt, Not Bold

Formatted: Indent: First line: 0"

Formatted: Font: Not Bold, Italic

Formatted: Font: (Default) Times New Roman, 12 pt, Not Bold

771 geologically complex areas. This highlights both the importance of strategic calibration point  
772 distribution and the robustness of the CSAMT-based approach, even with limited borehole data.  
773 Future efforts could improve efficiency by adapting borehole placement based on preliminary  
774 CSAMT results, optimizing both calibration and cost.

#### 775 **4.13 Rationale for variable CSAMT profile extents**

Formatted: Font: Bold

776 The variation in CSAMT profile lengths reflects site-specific logistical and geological  
777 constraints encountered during field deployment. Factors such as terrain accessibility,  
778 infrastructure (e.g., roads, buildings), and the need to capture key geological features (e.g., faults,  
779 lithological boundaries) influenced the extent of each profile. In some cases, shorter profiles  
780 were required due to rugged topography or land access limitations, while longer profiles were  
781 employed where feasible to ensure adequate coverage across broader structural domains. Despite  
782 the variation in length, all profiles were designed to achieve sufficient depth penetration and  
783 resolution for reliable resistivity–permeability modeling, as validated through borehole  
784 calibration.

Formatted: Font: (Default) Times New Roman, 12 pt, Not Bold

Formatted: Indent: First line: 0"

#### 785 **4.14 Addressing the borehole–CSAMT depth discrepancy**

786 Although the borehole data used for calibration were limited to depths of 0–200 m, this interval  
787 encompasses key lithological units, granite, hornstone, and sandstone, and captures a  
788 representative range of resistivity and  $k$  conditions. These near-surface measurements provided a  
789 robust basis for developing the empirical resistivity–permeability ( $k$ – $\rho$ ) relationship, which was  
790 subsequently applied across the full depth range of the CSAMT profiles (~1300 m). While direct  
791 validation at greater depths is not currently possible due to the absence of deep borehole data, the

Formatted: Indent: First line: 0"

Formatted: Font: Not Bold, Italic

792 extrapolation of the calibrated model is supported by consistent geological structure,  
793 hydrochemical data, and stratigraphic continuity reported by the Geological Survey of China  
794 down to ~1000 m. Furthermore, strong spatial alignment between resistivity, inferred  $k$ , and  
795 mapped lithological boundaries lends confidence to the model's deeper projections. We  
796 acknowledge this depth mismatch as a limitation, but emphasize that the approach enables  
797 meaningful  $k$  estimation in data-scarce regions. Future studies incorporating deep drilling and in-  
798 situ petrophysical logging will be essential to further refine model accuracy at greater depths.

Formatted: Font: Not Bold, Italic

Formatted: Font: Not Bold, Italic

Formatted: Font: (Default) Times New Roman, 12 pt

#### 799 **4.15 Ground-truthing CSAMT with regional geological frameworks**

800 Our results show strong agreement with regional geological and hydrogeological data from local  
801 and national surveys, confirming the reliability of the integrated CSAMT–borehole approach.  
802 This alignment supports the method’s scientific validity and scalability for  $k$  estimation in  
803 structurally complex, data-scarce settings. While grounded in established geophysical principles,  
804 the strength of this study lies in its site-specific integration of deep  $k$  modeling, field validation,  
805 and empirical calibration. Overall, the findings highlight CSAMT’s potential as a practical tool  
806 for deep groundwater exploration and sustainable resource management.

### 807 **5 Conclusions**

808 This study introduces a novel, non-invasive methodology for deep groundwater investigation  
809 using CSAMT, applied for indirect estimation of 2D and 3D  $k$  distributions in complex hard rock  
810 terrains at depths reaching 1300 m. While borehole drilling remains the conventional means of  
811 evaluating hydraulic parameters, its high cost, limited spatial coverage, and logistical challenges  
812 restrict its broader applicability. Our approach leverages co-located CSAMT and borehole data

813 to construct an empirical resistivity–permeability relationship, enabling the generation of  
814 spatially continuous hydrogeological models that extend beyond the reach of direct sampling.

815 Although the CSAMT method is inherently based on ill-posed inversion and relies on  
816 assumptions during model construction, the integration of borehole-derived ground truth allows  
817 for the calibration and partial validation of subsurface predictions. The resulting  $k$  models align  
818 well with regional geological features and stratigraphy. For instance, high- $k$  sandstone zones  
819 ( $<350 \Omega\text{m}$ , 10–20 mD) contrast distinctly with low- $k$  granite zones ( $>700 \Omega\text{m}$ , 0–5 mD),  
820 supporting the underlying physical relationships inferred from the data. These 2D/3D models  
821 reveal promising groundwater zones below 700 m in central regions and around granite  
822 boundaries down to 1300 m. While this study demonstrates the potential of CSAMT to enhance  
823 hydrogeological understanding in data-sparse regions, it is important to emphasize that the  
824 predictive accuracy of the models depends critically on the availability and quality of borehole  
825 data for empirical calibration.

826 Future work should focus on expanding the empirical dataset, integrating additional  
827 geophysical measurements, and validating models across diverse geological settings to improve  
828 generalizability. Ultimately, this combined geophysical–borehole approach holds promise for  
829 cost-effective and scalable groundwater assessment in geologically challenging environments,  
830 provided that its limitations and dependencies are clearly understood and addressed.

### 831 **Code availability**

832 Software application or custom code supports the published claims and complies with field  
833 standards

### 834 **Data availability**

835 Data available on request from the corresponding author

836 **Author contributions**

837 MH conceptualized the research goals and developed the methodology. MH and LS found the  
838 funding for the project. MH developed the code and prepared its visualization, and LS provided  
839 programming support and analysis tools. MH prepared the original draft.

840 **Declaration of competing interest**

841 The authors declare that they have no conflict of interest.

842 **Acknowledgements**

843 The authors gratefully acknowledge the support provided by the State Key Laboratory of  
844 Mountain Hazards and Engineering Resilience, Institute of Mountain Hazards and Environment,  
845 Chinese Academy of Sciences, and the China-Pakistan Joint Research Center on Earth Sciences,  
846 CAS-HEC, Islamabad, Pakistan.

847 **Financial support**

848 This research was financially supported by the National Natural Science Foundation of China  
849 (Grant No. U22A20603), the International Science and Technology Cooperation Program of  
850 Shanghai Cooperation Organization, Science and Technology Department, Xinjiang, China  
851 (Grant No. E202301005), and the National Natural Science Foundation of China's Research  
852 Fund for International Young Scientists (RFIS-I) (Grant No. 42350410442).

853 **References**

- 854 1. Abbas, M., Deparis, J., Isch, A., Mallet, C., Jodry, C., Azaroual, M., Abbar, B., and  
855 Baltassat, J.M.: Hydrogeophysical characterization and determination of petrophysical  
856 parameters by integrating geophysical and hydrogeological data at the limestone vadose  
857 zone of the Beauce aquifer, *Journal of Hydrology*, 615, 128725, 2022.  
858 <https://doi.org/10.1016/j.jhydrol.2022.128725>.
- 859 2. Allègre, V., Brodsky, E.E., Xue, L., Nale, S.M., Parker, B.L., and Cherry, J.A.: Using  
860 earth-tide induced water pressure changes to measure in situ permeability: A comparison  
861 with long-term pumping tests, *Water Resour. Res.*, 52(4), 3113–3126, 2016.  
862 <https://doi.org/10.1002/2015WR017346>.
- 863 3. Amiotte Suchet, P., Probst, J.L., and Ludwig, W.: Worldwide distribution of continental  
864 rock lithology: Implications for the atmospheric/ soil CO<sub>2</sub> uptake by continental  
865 weathering and alkalinity river transport to the oceans, *Glob Biogeochem Cycles*, 17,  
866 1038, 2003. <https://doi.org/10.1029/2002GB001891>.
- 867 ~~4. An, Z., and Di, Q.: Investigation of geological structures with a view to HLRW disposal,  
868 as revealed through 3D inversion of aeromagnetic and gravity data and the results of  
869 CSAMT exploration, *Journal of Applied Geophysics*, 135, 204–211, 2016.~~
- 870 ~~5.4.~~ Archie, G.E.: The electrical resistivity log as an aid in determining some reservoir  
871 characteristics, *Transactions of the AIME*, 146(1), 54–62, 1942.  
872 <https://doi.org/10.2118/942054-G>.
- 873 ~~6.5.~~ Asfahani, J.: Estimation of the hydraulic parameters by using an alternative vertical  
874 electrical sounding technique: case study from semiarid Khanasser valley region  
875 Northern Syria, *Acta Geophys*, 71, 997–1013, 2023. [https://doi.org/10.1007/s11600-022-](https://doi.org/10.1007/s11600-022-00926-0)  
876 [00926-0](https://doi.org/10.1007/s11600-022-00926-0).

877 ~~7.6.~~ ASTM.: Standard Test Methods for Measurement of Hydraulic Conductivity of Saturated  
878 Porous Materials Using a Flexible Wall Permeameter (ASTM D5084-21), ASTM  
879 International, 2021. [DOI: 10.1520/D5084-21](https://doi.org/10.1520/D5084-21).

880 ~~8. Bai, D., Unsworth, M., Meju, M., Ma, X., Teng, J., Kong, X., Sun, Y., Sun, J., Wang, L.,~~  
881 ~~Jiang, C., Zhao, C., Xiao, P., and Liu, M.: Crustal deformation of the eastern Tibetan~~  
882 ~~plateau revealed by magnetotelluric imaging, Nature Geosci., 3, 358–362, 2010.~~

883 ~~9.7.~~ Bauer-Gottwein, P., Gondwe, B.N., Christiansen, L., Herckenrath, D., Kgotlhang, L., and  
884 [Zimmermann, S.: Hydrogeophysical exploration of three-dimensional salinity anomalies](#)  
885 [with the time domain electromagnetic method \(TDEM\), J. Hydrol., 380\(3–4\), 318–329,](#)  
886 [2010. https://doi.org/10.1016/j.jhydrol.2009.11.007](https://doi.org/10.1016/j.jhydrol.2009.11.007).

887 ~~10.8.~~ Bear, J.: Dynamics of Fluids in Porous Media. New York: American Elsevier  
888 Publishing Company, 1972.

889 ~~11. Bentley, L.R., and Gharibi, M.: Two- and three-dimensional electrical resistivity imaging~~  
890 ~~at a heterogeneous remediation site, Geophysics, 69, 674–680, 2004.~~

891 ~~12. Binley, A., and Kemna, A.: DC resistivity and induced polarization methods, In~~  
892 ~~Hydrogeophysics, Springer, pp. 129–156, 129–2005.~~

893 ~~9. Binley, A., Cassiani, G., and Deiana, R.: Hydrogeophysics: opportunities and challenges,~~  
894 ~~Bollettino Di Geofisica Teorica Ed Applicata, 51(4), 267–287, 2010. [Online]. Available:~~  
895 ~~[http://www.scopus.com/inward/record.url?eid=2-s2.0-](http://www.scopus.com/inward/record.url?eid=2-s2.0-78650438167&partnerID=40&md5=96e14979c82f4b23e8fed0ac0140e7db)~~  
896 ~~[78650438167&partnerID=40&md5=96e14979c82f4b23e8fed0ac0140e7db](http://www.scopus.com/inward/record.url?eid=2-s2.0-78650438167&partnerID=40&md5=96e14979c82f4b23e8fed0ac0140e7db).~~

897 ~~10. Binley, A., Hubbard, S.S., Huisman, J.A., Revil, A., Robinson, D.A., Singha, K., and~~  
898 ~~Slater, L.D.: The emergence of hydrogeophysics for improved understanding of~~

**Formatted:** Font: (Default) Times New Roman, 12 pt

**Formatted:** Indent: Left: 0.5", No bullets or numbering

**Formatted:** Font: (Default) Times New Roman, 12 pt, Not Bold, No underline, Font color: Auto

**Formatted:** List Paragraph, Justified, Numbered + Level: 1 + Numbering Style: 1, 2, 3, ... + Start at: 1 + Alignment: Left + Aligned at: 0.25" + Indent at: 0.5"

**Formatted:** Font: (Default) Times New Roman, 12 pt, Not Bold, No underline, Font color: Auto

- 899 [subsurface processes over multiple scales, \*Water Resources Research\*, 51\(6\), 3837–3866,](#)  
900 [2015. <https://doi.org/10.1002/2015WR017016>.](#)
- 901 ~~13-11.~~ Borah, U.K., and Patro, P.K.: Estimation of the depth of investigation in the  
902 magnetotelluric method from the phase, *Geophysics*, 84 (6), E377–E385, 2019.  
903 <https://doi.org/10.1190/geo2018-0124.1>.
- 904 ~~14-12.~~ Brace, W.F., Walsh, J.B., and Frangos, W.T.: Permeability of granite under high  
905 pressure, *Journal of Geophysical Research*, 73(6), 2225–2236, 1968.  
906 <https://doi.org/10.1029/JB073i006p02225>.
- 907 ~~15-13.~~ Cagniard, L.: Basic theory of the magneto-telluric method of geophysical  
908 prospecting, *Geophysics*, 18 (3), 605–635, 1953. <https://doi.org/10.1190/1.1437915>.
- 909 ~~16. Camporese, M., Cassiani, G., Deiana, R., and Salandin, P.: Assessment of local hydraulic~~  
910 ~~properties from electrical resistivity tomography monitoring of a three-dimensional~~  
911 ~~synthetic tracer test experiment, *Water Resources Research*, 47 (12), 2011.~~
- 912 ~~17-14.~~ Carbillet, L., Griffiths, L., Heap, M.J., Duwiquet, H., Baud, P., Violay, M.E.S.,  
913 Reuschlé, T., and Guillou-Frottier, L.: The Influence of Micro- and Macrocracks on the  
914 Permeability of Granite, *Rock Mech Rock Eng*, 58, 1361–1378, 2024.  
915 <https://doi.org/10.1007/s00603-024-04174-0>.
- 916 ~~15.~~ Carman, P.C.: *Flow of Gases through Porous Media*, Academic Press, New York;  
917 Butterworths, London, 1956. 182 pp. Illus, 1956. DOI: [10.1126/science.124.3234.1254.b](https://doi.org/10.1126/science.124.3234.1254.b).
- 918 ~~18-16.~~ Chapuis, R.P., and Aubertin, M.: *Predicting the Coefficient of Permeability of*  
919 *Soils Using the Kozeny-Carman Equation*. École Polytech. Montréal, 2003, [Online].  
920 [Available: http://publications.polymtl.ca/2605/](http://publications.polymtl.ca/2605/)

Formatted: Font: (Asian) Times New Roman

921 ~~19. Clennell, M.B.: Tortuosity: a guide through the maze, Geological Society, London,~~  
922 ~~Special Publications, 122(1), 299–344, 1997.~~

923 ~~17. Condon, L.E., Markovich, K.H., Kelleher, C.A., McDonnell, J.J., Ferguson, G., and~~  
924 ~~McIntosh, J.C.: Where Is the Bottom of a Watershed? Water Resources Research, 56(3),~~  
925 ~~e2019WR026010, 2020. <https://doi.org/10.1029/2019WR026010>.~~

926 ~~20. Courtois, N., Dewandel, B., Bhuvana, V., Ahmed, S., and Chandra, S.: Contribution of~~  
927 ~~vertical and horizontal fractures to the groundwater flow in crystalline hard rock aquifers:~~  
928 ~~Insights from a comparative study of three different sites in southern India,~~  
929 ~~Hydrogeology Journal, 18(8), 1811–1827, 2010.~~

930 ~~18. Daily, W., Ramirez, A., LaBrecque, D., and Nitao, J.: Electrical resistivity tomography of~~  
931 ~~vadose water movement, Water Resources Research, 28(5), 1429–1442, 1992.~~  
932 ~~<https://doi.org/10.1029/91WR03087>.~~

933 ~~21. De Lima, O.A.L., and Niwas, S.: Estimation of hydraulic parameters of shaly sandstone~~  
934 ~~aquifers from geological measurements, J Hydrol, 235, 12–26, 2000.~~

935 ~~22-19.~~ Dell'Oca, A., Guadagnini, A., and Riva, M.: Interpretation of multi-scale  
936 permeability data through an information theory perspective, Hydrol. Earth Syst. Sci., 24,  
937 3097–3109, 2020. <https://doi.org/10.5194/hess-24-3097-2020>.

938 ~~23-20.~~ Dewandel, B., Lachassagne, P., Wyns, R., Maréchal, J.C., and Krishnamurthy,  
939 N.S.: A generalized 3-D geological and hydrogeological conceptual model of granite  
940 aquifers controlled by single or multiphase weathering, Journal of Hydrology, 330(1–2),  
941 260–284, 2006. <https://doi.org/10.1016/j.jhydrol.2006.03.026>.

942 ~~24-21.~~ Di, Q., Fu, C., An, Z., Wang, R., Wang, G., Wang, M., Qi, S., and Liang, P.: An  
943 application of CSAMT for detecting weak geological structures near the deeply buried

**Formatted:** Font: (Default) Times New Roman, 12 pt, Not Bold, No underline, Font color: Auto

**Formatted:** List Paragraph, Justified, Numbered + Level: 1 + Numbering Style: 1, 2, 3, ... + Start at: 1 + Alignment: Left + Aligned at: 0.25" + Indent at: 0.5"

**Formatted:** Font: (Default) Times New Roman, 12 pt, Not Bold, No underline, Font color: Auto

**Formatted:** List Paragraph, Justified, Numbered + Level: 1 + Numbering Style: 1, 2, 3, ... + Start at: 1 + Alignment: Left + Aligned at: 0.25" + Indent at: 0.5"

944 long tunnel of the Shijiazhuang-Taiyuan passenger railway line in the Taihang Mountains,  
945 Engineering Geology, 268, 105517, 2020. <https://doi.org/10.1016/j.enggeo.2020.105517>.

946 ~~25-22.~~ Esmailpour, M., Ghanbarian, B., Sousa, R., Peter, R., and King, P.R.: Estimating  
947 Permeability and Its Scale Dependence at Pore Scale Using Renormalization Group  
948 Theory, Water Resources Research, 59 (5), e2022WR033462, 2023.  
949 <https://doi.org/10.1029/2022WR033462>.

950 ~~26. Faybishenko, B., Witherspoon, P.A., and Benson, S.M.: Fracture matrix interaction in~~  
951 ~~unsaturated fractured rock: Experimental observations and modeling, Journal of~~  
952 ~~Contaminant Hydrology, 46(3-4), 223-256, 2000.~~

953 ~~27-23.~~ Ferguson, G., McIntosh, J.C., Jasechko, S., Kim, J.H., Famiglietti, J.S., and  
954 McDonnell, J.J.: Groundwater deeper than 500 m contributes less than 0.1% of global  
955 river discharge, Communication Earth and Environment, 4, 48, 2023.  
956 <https://doi.org/10.1038/s43247-023-00697-6>.

957 ~~28-24.~~ Fernando, A., and Pacheco, L.: Regional groundwater flow in hard rocks, Science  
958 of the Total Environment, 506-507, 182-195, 2015.  
959 <https://doi.org/10.1016/j.scitotenv.2014.11.008>.

960 ~~25. Ferré, T., Bentley, L., Binley, A., Linde, N., Kemna, A., Singha, K., Holliger,~~  
961 ~~k., Huisman, J.A., Minsley, B.: Critical Steps for the Continuing Advancement of~~  
962 ~~Hydrogeophysics. Eos, Transactions American Geophysical Union, 90(23), 200, 2009.~~  
963 ~~<https://doi.org/10.1029/2009EO230004>.~~

964 ~~29-26.~~ Fiandaca, G., Maurya, P.K., Balbarini, N., Hördt, A., Christiansen, A.V., Foged,  
965 N., Bjerg, P.L., and Auken, E.: Permeability estimation directly from logging-while-

**Formatted:** Font: (Default) Times New Roman, 12 pt, Not Bold, No underline, Font color: Auto

**Formatted:** List Paragraph, Justified, Numbered + Level: 1 + Numbering Style: 1, 2, 3, ... + Start at: 1 + Alignment: Left + Aligned at: 0.25" + Indent at: 0.5"

**Field Code Changed**

**Field Code Changed**

**Field Code Changed**

**Formatted:** Font: (Default) Times New Roman, 12 pt

**Formatted:** Font: (Default) Times New Roman, 12 pt

**Formatted:** Font: (Default) Times New Roman, 12 pt, No underline, Font color: Auto

966 drilling induced polarization data, *Water Resources Research*, 54, 2851–2870,  
967 2018. <https://doi.org/10.1002/2017WR022411>.

968 ~~30-27.~~ Fu, C., Di, Q., and An, Z.: Application of the CSAMT method to groundwater  
969 exploration in a metropolitan environment, *Geophysics*, 78 (5), B201–B209, 2013.  
970 <https://doi.org/10.1190/geo2012-0533.1>.

971 ~~31-28.~~ Fusheng, G., Haiyan, Y., Zengqian, H., Zhichun, W., Ziyu, L., Guocan, W., Linfu,  
972 X., Ye, G., and Wanpeng, Z.: Structural setting of the Zoujiashan-Julong'an region,  
973 Xiangshan volcanic basin, China, interpreted from modern CSAMT data, *Ore Geology*  
974 *Reviews*, 150, 105180, 2022. <https://doi.org/10.1016/j.oregeorev.2022.105180>.

975 ~~32-29.~~ Gerke, H.H., Dusek, J., and Vogel, T.: Mass transfer effects in 2-D dual-  
976 permeability modeling of field preferential bromide leaching with drain effluent, *Hydrol.*  
977 *Earth Syst. Sci. Discuss.*, 8, 5917–5967, 2011. <https://doi.org/10.5194/hessd-8-5917-2011>.

978 ~~33-30.~~ Gleeson, T., Moosdorf, N., Hartmann, J., and van Beek, L.P.H.: A glimpse  
979 beneath earth's surface: Global hydrogeology maps (GLHYMPS) of permeability and  
980 porosity, *Geophysical Research Letters*, ~~4341(211)~~, ~~43891–3898~~, ~~2016~~2014.  
981 <https://doi.org/10.1002/2014GL059856>.

982 31. Glover, P.W.J.: Geophysical properties of the near surface Earth: electrical properties,  
983 *Treatise on Geophysics*, 11, 89–137, 2015. DOI: 10.1016/B978-0-444-53802-4.00189-5.

984 ~~34-32.~~ Glover, P.W.J.: What is the cementation exponent? A new interpretation, *The*  
985 *Leading Edge*, 28(1), 82–85, 2009. <https://doi.org/10.1190/1.3064150>.

986 33. Gonzalez-Duque, D., Gomez-Velez, J.D., Person, M.A., Kelley, S., Key, K., and Lucero,  
987 D.: Groundwater Circulation Within the Mountain Block: Combining Flow and Transport  
988 Models With Magnetotelluric Observations to Untangle Its Nested Nature, *Water*

**Formatted:** Font: (Default) Times New Roman, 12 pt

**Formatted:** Font: (Default) Times New Roman, 12 pt, No underline, Font color: Auto  
**Formatted:** List Paragraph, Justified, Numbered + Level: 1 + Numbering Style: 1, 2, 3, ... + Start at: 1 + Alignment: Left + Aligned at: 0.25" + Indent at: 0.5"

989 Resources Research, 60(4), e2023WR035906, 2024,  
990 <https://doi.org/10.1029/2023WR035906>.

991 ~~35-34.~~ Hasan, M., and Shang, Y.: Geophysical evaluation of geological model  
992 uncertainty for infrastructure design and groundwater assessments, Engineering Geology,  
993 299, 106560, 2022. <https://doi.org/10.1016/j.enggeo.2022.106560>.

994 ~~36-35.~~ Hasan, M., Shang, Y., Jin, W., and Akhter, G.: Estimation of hydraulic  
995 parameters in a hard rock aquifer using integrated surface geoelectrical method and  
996 pumping test data in southeast Guangdong China, Geosci J, 25 (2), 223–242, 2021.  
997 <https://doi.org/10.1007/s12303-020-0018-7>.

998 ~~37-36.~~ Hasan, M., Su, L., Cui, P., and Shang, Y.: Development of deep-underground  
999 engineering structures via 2D and 3D RQD prediction using non-invasive  
1000 CSAMT, Scientific Reports, 15, 1403, 2025. <https://doi.org/10.1038/s41598-025-85626-7>.

1001 ~~37.~~ [Herckenrath, D., Auken, E., Christiansen, L., Behroozmand, A.A., and Bauer - Gottwein,](#)  
1002 [P.: Coupled hydrogeophysical inversion using time-lapse magnetic resonance sounding](#)  
1003 [and time-lapse gravity data for hydraulic aquifer testing: Will it work in practice? Water](#)  
1004 [Resources Research, 48\(1\), W01539, 2012. <https://doi.org/10.1029/2011WR010411>.](#)

1005 ~~38.~~ [Herckenrath, D., Odlum, N., Nenna, V., Knight, R., Auken, E., and Bauer - Gottwein, P.:](#)  
1006 [Calibrating a Salt Water Intrusion Model with Time-Domain Electromagnetic Data,](#)  
1007 [Groundwater, 51\(3\), 385–397, 2013. <https://doi.org/10.1111/j.1745-6584.2012.00974.x>.](#)

1008 ~~39.~~ [Hinnell, A.C., Ferré, T.P.A., Vrugt, J.A., Huisman, J.A., Moysey, S., Rings, J., and](#)  
1009 [Kowalsky, M.B.: Improved extraction of hydrologic information from geophysical data](#)  
1010 [through coupled hydrogeophysical inversion, Water Resources Research, 46\(4\), W00D40,](#)  
1011 [2010. <https://doi.org/10.1029/2008WR007060>.](#)

**Formatted:** Font: (Default) Times New Roman, 12 pt, No underline, Font color: Auto

**Formatted:** List Paragraph, Justified, Numbered + Level: 1 + Numbering Style: 1, 2, 3, ... + Start at: 1 + Alignment: Left + Aligned at: 0.25" + Indent at: 0.5"

**Formatted:** Font: (Default) Times New Roman, 12 pt, No underline, Font color: Auto

**Formatted:** Font: (Default) Times New Roman, 12 pt, No underline, Font color: Auto

**Formatted:** Font: (Default) Times New Roman, 12 pt, No underline, Font color: Auto

**Formatted:** Font: (Default) Times New Roman, 12 pt, No underline, Font color: Auto

1012 ~~38-40.~~ Hu, X.Y., Peng, R.H., Wu, G.J., Wang, W.P., Huo, G.P., and Han, B.: Mineral  
1013 exploration using CSAMT data: application to Longmen region metallogenic belt,  
1014 Guangdong Province, China, *Geophysics*, 78, B111–B119, 2013.  
1015 <https://doi.org/10.1190/geo2012-0115.1>.

1016 ~~39. Hubbard, S.H., and Rubin, Y.: Hydrogeological parameter estimation using geophysical~~  
1017 ~~data: a review of selected techniques, *J Contam Hydrol*, 45 (3), 34, 2002.~~

1018 ~~41. Ingebritsen, S.E., and Manning, C.E.: Permeability of the continental crust: dynamic~~  
1019 ~~variations inferred from seismicity and metamorphism, *Geofluids*, 10, 193–205, 2010.~~  
1020 ~~<https://doi.org/10.1111/j.1468-8123.2010.00278.x>.~~

1021 ~~40-42.~~ ISRM.: Suggested methods for rock characterization, testing and monitoring:  
1022 2007–2014, Springer, 2015. <https://doi.org/10.1007/978-3-319-07713-0>.

1023 ~~41. Jardani, A., Revil, A., Dupont, J. P., and Benderitter, Y.: Detection of preferential~~  
1024 ~~groundwater pathways in sinkhole fields using self potential methods, *Journal of*~~  
1025 ~~*Hydrology*, 335(1–2), 187–199, 2007.~~

1026 ~~43. Jardani, A., Revil, A., Santos, F., Fauchard, C., and Dupont, J.P.: Detection of~~  
1027 ~~preferential infiltration pathways in sinkholes using joint inversion of self - potential and~~  
1028 ~~EM - 34 conductivity data, *Geophysical Prospecting*, 55(5), 749–760, 2007.~~  
1029 ~~<https://doi.org/10.1111/j.1365-2478.2007.00638.x>.~~

1030 ~~42-44.~~ Jasechko, S., Seybold, H., Perrone, D., Fan, Y., Shamsudduha, M., Taylor, R.G.,  
1031 Fallatah, O., and Kirchner, J.W.: Rapid groundwater decline and some cases of recovery  
1032 in aquifers globally, *Nature*, 625, 715–721, 2024. [https://doi.org/10.1038/s41586-023-](https://doi.org/10.1038/s41586-023-06879-8)  
1033 [06879-8](https://doi.org/10.1038/s41586-023-06879-8).

**Formatted:** Font: (Default) Times New Roman, 12 pt, No underline, Font color: Auto

**Formatted:** List Paragraph, Justified, Numbered + Level: 1 + Numbering Style: 1, 2, 3, ... + Start at: 1 + Alignment: Left + Aligned at: 0.25" + Indent at: 0.5"

**Formatted:** Font: (Default) Times New Roman, 12 pt, No underline, Font color: Auto

**Formatted:** List Paragraph, Justified, Numbered + Level: 1 + Numbering Style: 1, 2, 3, ... + Start at: 1 + Alignment: Left + Aligned at: 0.25" + Indent at: 0.5"

1034 ~~45. Jiang, X.W., Wan, L., Wang, J.Z., Yin, B.X., Fu, W.X., and Lin, C.H.: Field~~  
1035 ~~identification of groundwater flow systems and hydraulic traps in drainage basins using a~~  
1036 ~~geophysical method, Geophysical Research Letters, 41(8), 2812–2819, 2014.~~  
1037 ~~<https://doi.org/10.1002/2014GL059579>.~~

1038 ~~43. Jiang, Y., Wu, X., and Shi, Z.: A novel model to estimate permeability from~~  
1039 ~~formation resistivity, Journal of Petroleum Science and Engineering, 124, 15–23, 2014.~~

1040 ~~44-46. Kouadio, K.L., Liu, R., Malory, A.O., and Liu, C.: A novel approach for water~~  
1041 ~~reservoir mapping using controlled source audio-frequency magnetotelluric in Xingning~~  
1042 ~~area, Hunan Province, China, Geophysical Prospecting, 71, 1708–1727, 2023.~~  
1043 ~~<https://doi.org/10.1111/1365-2478.13385>.~~

1044 ~~45. Lachassagne, P., Wyns, R., and Dewandel, B.: The fracture permeability in hard rocks~~  
1045 ~~aquifers and its dynamic modeling: An integrated conceptual model of weathered~~  
1046 ~~crystalline aquifers, Hydrogeology Journal, 29(1), 1–20, 2021.~~

1047 ~~46-47. Laghari, A.N., Vanham, D., and Rauch, W.: The Indus basin in the framework of~~  
1048 ~~current and future water resources management, Hydrology and Earth System~~  
1049 ~~Sciences, 16 (4), 1063–1083, 2012. <https://doi.org/10.5194/hess-16-1063-2012>.~~

1050 ~~47. Lin, C.H., Lin, C.P., Hung, Y.C., Chung, C.C., Wu, P.L., and Liu, H.C.:~~  
1051 ~~Application of geophysical methods in a dam project: Life cycle perspective and Taiwan~~  
1052 ~~experience, Journal of Applied Geophysics, 158, 82–92, 2018.~~

1053 ~~48. Liu, X., Zhang, Y., and Zhang, D.: Permeability characteristics of fractured granite under~~  
1054 ~~varying stress conditions, Rock Mechanics and Rock Engineering, 54(3), 937–952, 2021.~~

1055 ~~49-48. Majumdar, R.K., and Das, D.: Hydrological characterization and estimation of~~  
1056 ~~aquifer properties from electrical sounding data in Sagar Island region, South 24~~

**Formatted:** Font: (Default) Times New Roman, 12 pt, No underline, Font color: Auto

**Formatted:** List Paragraph, Justified, Numbered + Level: 1 + Numbering Style: 1, 2, 3, ... + Start at: 1 + Alignment: Left + Aligned at: 0.25" + Indent at: 0.5"

**Formatted:** Indent: Left: 0.5", No bullets or numbering

**Formatted:** Indent: Left: 0.5", No bullets or numbering

1057 Parganas, West Bengal, India, Asian J Earth Sci, 4, 60–74, 2011.  
1058 <http://dx.doi.org/10.3923/ajes.2011.60.74>.

1059 ~~49. Manning, C.E., and Ingebritsen, S.E.: Permeability of the continental crust: Implications~~  
1060 ~~of geothermal data and metamorphic systems, Reviews of Geophysics, 37(1), 127–150,~~  
1061 ~~1999. <https://doi.org/10.1029/1998RG900002>.~~

1062 ~~50. Margat, J., and van der Gun, J.: Groundwater around the world: A geographic synopsis.~~  
1063 ~~CRC Press, 2013. <https://doi.org/10.1201/b13977>.~~

1064 ~~51. McKeown, C., Haszeldine, R.S., and Couples, G.D.: Mathematical modelling of~~  
1065 ~~groundwater flow at Sellafield, UK. Engineering Geology, 52(3–4), 231–250, 1999.~~

1066 ~~52. Medici, G., Ling, F., and Shang, J.: Review of discrete fracture network characterization~~  
1067 ~~for geothermal energy extraction, Frontiers in Earth Science, 11, 1328397, 2023.~~

1068 ~~53-50. Mira Geoscience Ltd.: GOCAD Mining Suite 3D Geological Modeling Software.~~  
1069 ~~Nancy University, Lorraine, France, 1999.~~

1070 ~~54. MOHURD (Ministry of Housing and Urban Rural Development of the People's Republic~~  
1071 ~~of China): National Groundwater Resources Strategic Survey and Planning Guidelines~~  
1072 ~~(in Chinese). Beijing: China Geological Press, 2021.~~

1073 ~~55-51. Mudunuru, M.K., Cromwell, E.L.D., Wang, H., and Chen, X.: Deep learning to~~  
1074 ~~estimate permeability using geophysical data, Advances in Water Resources, 167,~~  
1075 ~~104272, 2022. <https://doi.org/10.1016/j.advwatres.2022.104272>.~~

1076 ~~56. Neuzil, C.E.: How permeable are clays and shales? Water Resources Research, 30(2),~~  
1077 ~~145–150, 1994.~~

1078 ~~57. Niu, G., Chen, M., and Fan, L.: Stress dependent permeability of fractured granite and its~~  
1079 ~~implications for enhanced geothermal systems, Geothermics, 64, 294–303, 2016.~~

**Formatted:** Font: (Default) Times New Roman, 12 pt, No underline, Font color: Auto

**Formatted:** List Paragraph, Justified, Numbered + Level: 1 + Numbering Style: 1, 2, 3, ... + Start at: 1 + Alignment: Left + Aligned at: 0.25" + Indent at: 0.5"

1080 ~~58-52.~~ Niwas, S., and De Lima, O.A.L.: Aquifer parameter estimation from surface  
1081 resistivity data, *Groundwater*, 41, 94–99, 2003. [https://doi.org/10.1111/j.1745-  
6584.2003.tb02572.x](https://doi.org/10.1111/j.1745-<br/>1082 6584.2003.tb02572.x).

1083 ~~59-53.~~ Nwosu, L.I., Nwankwo, C.N., and Ekine, A.S.: Geoelectric investigation of the  
1084 hydraulic properties of the aquiferous zones for evaluation of groundwater potentials in  
1085 the complex geological area of imostate, Nigeria, *Asian J Earth Sci*, 6, 1–15, 2013.  
1086 <https://scialert.net/abstract/?doi=ajes.2013.1.15>.

1087 ~~60. Paterson, M.S., and Wong, T.F.: Experimental Rock Deformation: The Brittle Field,  
1088 Springer, 2005.~~

1089 ~~61-54.~~ Pellet, H., Arfib, B., Henry, P., Tournon, S., and Gassier, G.: Mesoscale  
1090 permeability variations estimated from natural airflows in the decorated Cosquer Cave  
1091 (southeastern France), *Hydrol. Earth Syst. Sci.*, 28, 4035–4057, 2024.  
1092 <https://doi.org/10.5194/hess-28-4035-2024>.

1093 ~~62-55.~~ Phoenix Geophysics CMTPro, The Canadian Phoenix CMT Pro Version software  
1094 for CSAMT data processing. Toronto, Ontario, Canada, 2020.

1095 ~~63-56.~~ Phoenix Geophysics CSAMT-SW, The Canadian Phoenix CSAMT-SW Version  
1096 software for CSAMT data inversion. Toronto, Ontario, Canada, 2020.

1097 ~~57. Pollock, D., and Cirpka, O.A.: Fully coupled hydrogeophysical inversion of a laboratory  
1098 salt tracer experiment monitored by electrical resistivity tomography, *Water Resources  
1099 Research*, 48(1), W01505, 2012. <https://doi.org/10.1029/2011WR010779>.~~

1100 ~~64. Qian, H., Wang, Y., Zhang, Y., and Su, Y.: Advances in deep groundwater exploration  
1101 and management under climatic stress in arid regions of China, *Journal of Hydrology*,  
1102 626, 130234, 2024.~~

**Formatted:** Font: (Default) Times New Roman, 12 pt, No underline, Font color: Auto

**Formatted:** List Paragraph, Justified, Numbered + Level: 1 + Numbering Style: 1, 2, 3, ... + Start at: 1 + Alignment: Left + Aligned at: 0.25" + Indent at: 0.5"

**Formatted:** Font: (Default) Times New Roman, 12 pt, No underline, Font color: Auto

1103 ~~65-58.~~ Qin, X.: Application of Unwedge program to geological stability analysis of deep  
1104 buried deposits, *Comprehensive*, 8, 270–273, 2017 (In Chinese).

1105 ~~66. Refsgaard, J.C., Arbjerg-Nielsen, K., Drews, M., Halsnæs, K., Jeppesen, E., Madsen, H.,~~  
1106 ~~and Christensen, J.H.: The role of uncertainty in climate change adaptation strategies — A~~  
1107 ~~Danish water management example, *Mitigation and Adaptation Strategies for Global*~~  
1108 ~~*Change*, 18(3), 337–359, 2012.~~

1109 ~~59. Revil, A., and Cathles III, L.M.: Permeability of shaly sands, *Water Resources Research*,~~  
1110 ~~35(3), 651–662, 1999. <https://doi.org/10.1029/98WR02700>.~~

1111 ~~67. Revil, A., and Cathles, L.M.: Permeability of shaly sands, *Water Resources Research*,~~  
1112 ~~35(3), 651–662, 1999.~~

1113 ~~68. Roa-García, M.C., Brown, S., Schreier, H., and Lavkulich, L.M.: The role of land use and~~  
1114 ~~soils in regulating water flow in small headwater catchments of the Andes, *Water*~~  
1115 ~~*Resources Research*, 47(5), 2010.~~

1116 ~~69. Robinson, J., Slater, L., Johnson, T., Shapiro, A., Tiedeman, C., Ntarlagiannis, D.,~~  
1117 ~~Johnson, C., Day-Lewis, F., Lacombe, P., Imbrigiotta, T., and Lane, J.: Imaging~~  
1118 ~~pathways in fractured rock using three-dimensional electrical resistivity tomography,~~  
1119 ~~*Groundwater*, 54(2), 186–201, 2016.~~

1120 ~~70. Rodell, M., Velicogna, I., and Famiglietti, J.S.: Satellite-based estimates of~~  
1121 ~~groundwater depletion in India, *Nature*, 460(7258), 999–1002, 2009.~~

1122 ~~71-60.~~ Rodi, W., and Mackie, R.L.: Nonlinear conjugate gradients algorithm for 2-D  
1123 magnetotelluric inversion, *Geophysics*, 66(1), 174–187, 2001.  
1124 <https://doi.org/10.1190/1.1444893>.

**Formatted:** Font: (Default) Times New Roman, 12 pt, No underline, Font color: Auto

**Formatted:** Numbered + Level: 1 + Numbering Style: 1, 2, 3, ... + Start at: 1 + Alignment: Left + Aligned at: 0.25" + Indent at: 0.5"

**Formatted:** Indent: Left: 0.5", No bullets or numbering

1125 ~~4-61.~~ Saar, M.O., and Manga, M.: Depth dependence of permeability in the Oregon  
1126 Cascades inferred from hydrogeologic, thermal, seismic, and magmatic modeling  
1127 constraints, Journal of Geophysical Research, 109(B4), B04204, 2004.  
1128 <https://doi.org/10.1029/2003JB002855>  
1129 ~~72-62.~~ Simpson, F., and Bahr, K.: Practical magnetotellurics. Cambridge University  
1130 Press, Cambridge. 254 pp, 2005. <https://doi.org/10.1017/CBO9780511614095>.  
1131 ~~73-63.~~ Singh, K.P.: Nonlinear estimation of aquifer parameters from surficial resistivity  
1132 measurements, Hydrology and Earth System Sciences Discussions, 2 (3), 917–938, 2005.  
1133 <https://doi.org/10.5194/hessd-2-917-2005>.  
1134 ~~74.~~ Singh, R., Prasad, M., and Al Tahini, A.: A comparative study of electrical and hydraulic  
1135 properties in carbonate and siliciclastic rocks, Geophysical Journal International, 221(3),  
1136 1837–1855, 2020.  
1137 ~~75.~~ Sinha, R., Israil, M., and Singhal, D.C.: A hydrogeological model of the relationship  
1138 between geoelectric and hydraulic parameters of anisotropic aquifers, Hydrogeol J, 17,  
1139 495–503, 2009.  
1140 ~~76-64.~~ Smith, J.T., and Booker, J.R.: Rapid inversion of two- and three-dimensional  
1141 magnetotelluric data, Journal of Geophysical Research: Solid Earth, 96 (B3), 3905–3922,  
1142 1991. <https://doi.org/10.1029/90JB02416>.  
1143 ~~77-65.~~ Soupios, P.M., Kouli, M., Vallianatos, F., Vafidis, A., and Stavroulakis, G.:  
1144 Estimation of aquifer hydraulic parameters from surficial geophysical methods: a case  
1145 study of Keritis Basin in Chania (Crete–Greece), J Hydrol, 1, 122–131, 2007.  
1146 <https://doi.org/10.1016/j.jhydrol.2007.02.028>.

**Formatted:** Font: (Default) Times New Roman, 12 pt, No underline, Font color: Auto

**Formatted:** Numbered + Level: 1 + Numbering Style: 1, 2, 3, ... + Start at: 1 + Alignment: Left + Aligned at: 0.25" + Indent at: 0.5"

**Formatted:** Font: (Default) Times New Roman, 12 pt, No underline, Font color: Auto

**Formatted:** Font: (Default) Times New Roman, 12 pt, No underline, Font color: Auto

**Formatted:** Font: (Default) Times New Roman, 12 pt

- 1147 ~~78. Vouillamoz, J.M., Lawson, F.M.A., Yalo, N., and Desloires, M.: The use of magnetic~~  
1148 ~~resonance sounding for quantifying specific yield and transmissivity in hard rock aquifers:~~  
1149 ~~the example of Beni, J Appl Geophys, 107, 16–24, 2014.~~
- 1150 ~~79.66.~~ Wada, Y., Van Beek, L.P., Van Kempen, C.M., Reckman, J.W., Vasak, S., and  
1151 Bierkens, M.F.: Global depletion of groundwater resources, Geophysical Research  
1152 Letters, 37 (20), [L20402](#), 2010. <https://doi.org/10.1029/2010GL044571>.
- 1153 ~~80.67.~~ Wang, R., Yin, C., Wang, M., and Di, Q.: Laterally constrained inversion for  
1154 CSAMT data interpretation, Journal of Applied Geophysics, 121, 63–70, 2015.  
1155 <https://doi.org/10.1016/j.jappgeo.2015.07.009>.
- 1156 ~~81. Wang, W., Xie, X., Zhang, Y., Yang, J., and Liu, C.: Hydrogeological properties~~  
1157 ~~of fractured sandstones in southern China, Hydrogeology Journal, 22(5), 1127–1142,~~  
1158 ~~2014.~~
- 1159 ~~82.68.~~ Waxman, M.H., and Smits, L.J.M.: Electrical conductivities in oil-bearing shaly  
1160 sands, Society of Petroleum Engineers Journal, 8(02), 107–122, 1968.  
1161 <https://doi.org/10.2118/1863-A>.
- 1162 ~~83.69.~~ Webring, M.W.: MINC: A Gridding Program Based on Minimum Curvature: U.S.  
1163 Geological Survey Open File Report, 81–1224, p. 41p, 1981.  
1164 <https://doi.org/10.3133/ofr811224>.
- 1165 ~~84.70.~~ Worthington, S.R.H., Davies, G.J., and Alexander, E.C. Jr.: Enhancement of  
1166 bedrock permeability by weathering, Earth-Sci Rev, 160, 188–202, 2016.  
1167 <https://doi.org/10.1016/j.earscirev.2016.07.002>.

Formatted: Indent: Left: 0.5", No bullets or numbering

- 1168 ~~85. Wynn, J., Mosbrucker, A., Pierce, H., and Spicer, K.: Where is the hot rock and where is~~  
1169 ~~the ground water using CSAMT to map beneath and around Mount St. Helens, Journal of~~  
1170 ~~Environmental and Engineering Geophysics, 21, 79–87, 2016.~~
- 1171 ~~86. Yadav, G.S., and Singh, S.K.: Integrated resistivity surveys for delineation of fractures~~  
1172 ~~for ground water exploration in hard rock areas, Journal of Applied Geophysics, 62 (3),~~  
1173 ~~301–312, 2007.~~
- 1174 ~~87-71. \_\_\_\_\_ Yan, Y., Ma, L., Qian, J., Zhao, G., Fang, Y., Ma, H., and Wang, J.: Estimating~~  
1175 ~~permeability of rock fracture based on geometrical aperture using geoelectrical~~  
1176 ~~monitoring, Journal of Hydrology, 644, 132067, 2024.~~  
1177 ~~<https://doi.org/10.1016/j.jhydrol.2024.132067>.~~
- 1178 ~~88. Yang, H.Q., and Zhang, L.: Bayesian back analysis of unsaturated hydraulic parameters~~  
1179 ~~for rainfall induced slope failure: A review, Earth Science Reviews, 251, 104714, 2024.~~
- 1180 ~~89-72. \_\_\_\_\_ Yang, J., Zhang, H., and Cui, Z.: Stability Analysis and Countermeasures of Rock~~  
1181 ~~Block in Underground Cavern, Guangdong Water Resources and Hydropower 5, 23–27,~~  
1182 ~~2021 (In Chinese)~~
- 1183 ~~90. Zhang, F., Zhou, Z., Huang, Y., and Chen, Z.: Determining the Permeability of Fractured~~  
1184 ~~Rocks Based on Joint Mapping, Groundwater, 42, 509–515, 2004.~~
- 1185 ~~91. Zhang, J., Sirieix, C., Genty, D., Salmon, F., Verdet, C., Mateo, S., Xu, S., Bujan, S.,~~  
1186 ~~Devaux, L., and Larcanché, M.: Imaging hydrological dynamics in karst unsaturated~~  
1187 ~~zones by time lapse electrical resistivity tomography, Science of the Total Environment~~  
1188 ~~907, 168037, 2024.~~
- 1189 ~~92. Zhang, L., Yang, C., and Qin, S.: Evaluation of groundwater flow in granite using core-~~  
1190 ~~based permeability and fracture analysis, Journal of Hydrology, 585, 124775, 2020.~~

1191 ~~93-73.~~ Zhang, M., Farquharson, C.G., and Liu, C.: Improved controlled source audio-  
1192 frequency magnetotelluric method apparent resistivity pseudo-sections based on the  
1193 frequency and frequency-spatial gradients of electromagnetic fields, *Geophysical*  
1194 *Prospecting*, 69, 474–490, 2021. <https://doi.org/10.1111/1365-2478.13059>.

1195 ~~94. Zhao, Y., Xu, T., and Luo, G.: Statistical analysis of rock permeability variation in~~  
1196 ~~different lithologies, *Engineering Geology*, 239, 123–133, 2018.~~

1197 ~~95-74.~~ Zhu, L., Gong, H., Dai, Z., Guo, G., and Teatini, P.: Modeling 3-D permeability  
1198 distribution in alluvial fans using facies architecture and geophysical acquisitions, *Hydrol.*  
1199 *Earth Syst. Sci.*, 21, 721–733, 2017. <https://doi.org/10.5194/hess-21-721-2017>.

1200 ~~75.~~ Zonge, K.L., and Hughes, L.J.: Kenneth L. Zonge and Larry J. Hughes, (1991), "9.  
1201 Controlled Source Audio-Frequency Magnetotellurics," *Investigations in Geophysics*,  
1202 713–810, ~~1988~~1991. <https://doi.org/10.1190/1.9781560802686.ch9>.